



HAL
open science

Controls on the provenance of late Eocene to Quaternary Mozambique Channel shales (DSDP 25 Site 242)

Martin Roddaz, Martin Nauton-Fourteu, Roberto Ventura Santos, Elton Luiz
Dantas, G r me Calves

► To cite this version:

Martin Roddaz, Martin Nauton-Fourteu, Roberto Ventura Santos, Elton Luiz Dantas, G r me Calves.
Controls on the provenance of late Eocene to Quaternary Mozambique Channel shales (DSDP 25 Site
242). *Marine Geology*, 2020, 421, pp.106090. 10.1016/j.margeo.2019.106090 . hal-02425257

HAL Id: hal-02425257

<https://hal.science/hal-02425257>

Submitted on 7 Mar 2022

HAL is a multi-disciplinary open access archive for the deposit and dissemination of scientific research documents, whether they are published or not. The documents may come from teaching and research institutions in France or abroad, or from public or private research centers.

L'archive ouverte pluridisciplinaire **HAL**, est destin e au d p t et   la diffusion de documents scientifiques de niveau recherche, publi s ou non,  manant des  tablissements d'enseignement et de recherche fran ais ou  trangers, des laboratoires publics ou priv s.



Distributed under a Creative Commons Attribution - NonCommercial 4.0 International License

1 **Controls on the Provenance of late Eocene to Quaternary Mozambique Channel**
2 **shales (DSDP 25 Site 242)**

3 **Martin Roddaz^{1,2*}, Martin Nauton-Fourteu³, Roberto Ventura Santos², Elton Luiz Dantas² and**
4 **Gérôme Calves¹**

5 ¹ Géosciences-Environnement Toulouse, Université de Toulouse; UPS (SVT-OMP); CNRS; IRD; 14
6 Avenue Édouard Belin, F-31400 Toulouse, France

7 ² Laboratório de Geocronologia, Instituto de Geociências, Universidade de Brasília, Brasília, DF 70910-
8 000, Brazil

9 ³ Earth and Ocean Sciences and Irish Centre for Research in Applied Geosciences (iCRAG),
10 School of Natural Sciences, National University of Ireland, Galway, University Road, Galway, Ireland.

11 *Corresponding author: Martin Roddaz (martin.roddaz@get.omp.eu)

12

13 **Abstract**

14 Provenance determination of late Eocene to Quaternary sediments deposited at the DSDP 25 Site 242
15 may help to evaluate the mechanisms that have controlled the sediment deposition in the Mozambique
16 Channel . To determine the provenance of the clay fraction, we measure major and trace element
17 concentrations as well as strontium ($^{87}\text{Sr}/^{86}\text{Sr}$) and neodymium isotopic compositions (expressed as
18 $\epsilon_{\text{Nd}(0)}$) of thirty-six sedimentary samples from DSDP 25 Site 242 on the eastern flank of the Davie
19 Fracture Zone. Light Rare Earth Element (LREE) enrichment and Heavy REE (HREE) depletions
20 against Post Archean Australian Shales (PAAS) associated with Ce anomalies higher than or equal to
21 0.90 for all the analyzed samples suggest very little influence of authigenic smectite incorporation. The
22 absence of correlation of Al/Si and CIA with REE content, Eu/Eu*, Cr/Th, Th/Sc, and $^{87}\text{Sr}/^{86}\text{Sr}$ and
23 $\epsilon_{\text{Nd}(0)}$ suggests that chemical weathering has not modified these provenance proxies. Slight increase of
24 Eu/Eu*, Cr/Th ratios, $\epsilon_{\text{Nd}(0)}$ values associated with slight decrease in $^{87}\text{Sr}/^{86}\text{Sr}$ and Th/Sc ratios from
25 the late Eocene to the Quaternary point to input of less differentiated and younger detritus to the DSDP

26 25 Site 242 with age. Based on variations in $\epsilon_{Nd(0)}$ and Nd concentrations, we estimate an overall
27 decrease of the Southeast African rivers (Congo/Zambezi) contribution from $\sim 65.7\%$ (Standard
28 Deviation (S.D.) ~ 13.2) in the late Eocene to $\sim 28.5\%$ (S.D. ~ 10.0) in the early Pliocene. The causes
29 for the low $\epsilon_{Nd(0)}$ values and high Southeast African contribution between the late Eocene and the early
30 Oligocene remain to be determined. It could record the onset of modern sedimentation in the Zambezi
31 delta or the discharge of the Paleo Congo river in the Indian Ocean. The decrease of Zambezi
32 contribution between the late Oligocene and early Pliocene is attributed to the cumulative effect of
33 increasing tectonic activity of the Davie Fracture Zone and intensification of the Mozambique Current.
34 The late Pliocene to Quaternary glacial-interglacial cycles promoted higher Zambezi contribution
35 during glacial sea-level lowstands and in turn lower $\epsilon_{Nd(0)}$ detrital values, whereas low Zambezi
36 contributions are favored during interglacial highstand causing higher $\epsilon_{Nd(0)}$ values. Hence, the modern
37 dispersal pattern of fine-grained sediments within the Mozambique Channel is no younger than late
38 Pliocene.

39 **Introduction**

40 Provenance changes of clastic sediments deposited in deep offshore ocean settings may record
41 the denudation history of adjacent continents and consequently changes in paleorelief, drainage
42 configuration, as well as sediment transport associated with large-scale tectonic processes, climatic
43 change, and variation in paleo-oceanic current pathways. The provenance of deep-sea sediments has
44 been used to infer climate-driven changes in drainage sources during glacial-interglacial cycles
45 (Bonneau et al., 2017; van der Lubbe et al., 2016), to evaluate the effect of Quaternary glacial and
46 interglacial cycle on oceanic current intensities and paths (Fagel et al., 1999; Franzese et al., 2006;
47 Innocent et al., 1997; Revel et al., 1996), to evaluate the respective role of tectonics and climate in
48 sediment supply at geological timescale (Fagel et al., 1994), to reconstruct the evolution of continental
49 paleodrainage basins (Liu et al., 2017; Murlot et al., 2018) or even to unravel details about past deep
50 ocean circulation patterns during the Cretaceous (Murlot et al., 2018). With a few exceptions (e.g.
51 Murlot et al., 2018), most studies dealing with the provenance of deep-sea sediments concern present-

52 day to Pleistocene in age sediments. To date there is no provenance study of pre-Pleistocene
53 Mozambique Channel or basin sediments.

54 The Cenozoic sedimentary infill of the Mozambique Channel and Basin is controlled by the
55 variations in sediment supply, subsidence and oceanic near-bottom current intensities. Onshore, the
56 southern part of the African plateau was tectonically-reactivated during late Eocene to early Miocene
57 times (40–15 Ma; Baby et al., 2018), which may have resulted in an increase of Zambezi river detritus
58 exported to the Indian Ocean during Oligocene times (34–24 Ma, Walford et al., 2005). Also, this
59 might have cut off the hydrological connection of the Congo drainage basin with Indian Ocean in the
60 Oligocene or Eocene (30–40 Ma; Stankiewicz and de Wit, 2006). From late Miocene and onward,
61 drainage capture and doubling of the size of the Zambezi catchment during the Pliocene would have
62 also considerably increased the contribution of Zambezi river sediments to the Indian Ocean (Walford
63 et al., 2005). Meanwhile an offshore middle Miocene graben that was formed along the Davie Ridge
64 (Droz and Mougnot, 1987) as a result of the southerly extension of the East African Rifting System
65 since the Oligocene (Mahanjane, 2014) may have controlled the subsidence in the Mozambique
66 Channel. These may have influenced the variation in intensities of the Mozambique Current and its
67 effect on sediment deposition during the Cenozoic. One way to evaluate the influence of any of these
68 processes is to determine the provenance of well-dated siliciclastic sediments deposited in the
69 Mozambique Channel, at DSDP 25 Site 242. In detail, Nd isotopes may be particularly useful as they
70 have been extensively used as tracer of deep-sea sediment source (e.g. Goldstein and O’Nions; 1981;
71 Dia et al., 1992; Grousset et al., 1990, 1988; Murlot et al., 2018; Revel et al., 1996a,b). Furthermore,
72 present-day sediments deposited in the Mozambique Channel and basin have contrasting Nd isotopic
73 compositions (Fig.1). Indeed, sediments entering the Mozambique Channel from the North are
74 characterized by input of geologically-young material, which results in $\epsilon_{Nd(0)}$ values close to -11.2 (van
75 der Lubbe et al., 2016), whereas sediments deposited southward in the Mozambique Basin by the
76 Mozambique Current are characterized by lower $\epsilon_{Nd(0)}$ values (-15.5, Franzese et al., 2006) due to
77 contributions from relatively older source rock areas by the Zambezi river (Fig. 1).

78 The goal of this study is to determine the provenance of siliciclastic sediments deposited in the
79 Mozambique Channel, since the late Eocene based on the major and trace element concentrations and
80 Sr-Nd isotopic data of thirty-six clay samples of clay-rich sediments from the DSDP 25 Site 242 (Fig.
81 1). Determining the provenance of these sediments will provide new constraints on the geographical
82 source of the sediments deposited in the Mozambique Channel and how long-term geological
83 processes (drainage reorganization, tectonics of the East African Rift) may have controlled the
84 sediments deposited by the Mozambique Current.

85 **Geological settings and potential sediment sources**

86 2.1 Geological settings

87 The Deep Sea Drilling Project (DSDP) 25 Site 242 was drilled in 1972 and is located on the
88 eastern flank of the Davie Ridge (Simpson et al., 1974) in the Mozambique Channel at 2275 m water
89 depth. Site 242 is intermittently cored to 676 m depth providing late Eocene to Holocene sediments.
90 The Mozambique Channel is a broad trough bounded to the West by the Mozambique continental
91 slope and to the East by the Madagascar continental slope (Fig. 1). It hosts the inner part of the
92 Mozambique deep-sea fan and associated feeding canyons, the west-east Zambezi Valley, and the
93 north-south Serpa Pinto Valley (Droz and Mougénot, 1987; Kolla et al., 1980). The Mozambique
94 Channel is structurally partitioned by the asymmetric N-S trending Davie Ridge (Fig. 1). The Davie
95 Ridge often referred to as the Davie Fracture Zone (DFZ) is a shear zone that developed during the
96 southerly movement of East Gondwana between the middle Jurassic drift and the early Cretaceous
97 (Franke et al., 2015; Mahanjane, 2014; Mougénot et al., 1986). During its active phase, the DFZ
98 experienced pure strike-slip movement (Mahanjane, 2014). Since the Oligocene, southerly extension
99 of the DFZ has been related to the East African Rifting System (Deville et al., 2018; Franke et al.,
100 2015; Mahanjane, 2014).

101 The inner Mozambique Fan (also termed upper fan) is characterized by two main feeding paths
102 that have been successively dominant (Droz and Mougénot, 1987). From the Oligocene to early
103 Miocene, the inner fan was supplied by north Mozambique terrigenous sediments through the north-

104 south Serpa Pinto Valley. In contrast since the middle Miocene, the inner fan is mainly fed by
105 sediments transported by the Zambezi river through the west-east Zambezi Valley (Droz and
106 Mougenot, 1987). This change in sedimentary source was a consequence of a graben formation along
107 the Davie Ridge that may have led to the abandonment of the Serpa Pinto Valley (Droz and Mougenot,
108 1987). Estimates of the Zambezi sediment flux to the Indian Ocean indicate that there were two
109 periods of elevated sedimentary flux in the Cenozoic: i) during Oligocene times (34–24 Ma) as a
110 response of rapid regional uplift of Southern Africa and ii) from late Miocene times (~10 Ma) to
111 present-day due to a doubling of the size of the Zambezi catchment during the Pliocene, respectively
112 (Walford et al., 2005).

113 2.2. Modern and past oceanic circulation along the Mozambique Channel

114 The Mozambique Current (MC, Fig. 1) is the southern extent of the Northeast Madagascar
115 Current (NEMC, Fig.1), which corresponds to the northern branch of the South Equatorial Current
116 (SEC, Fig.1). The Mozambique Current is responsible for the strong, net southward flow along the
117 Mozambique Channel (Ridderinkhof et al., 2010). The flow through the Mozambique Channel occurs
118 through the passage of large anticyclonic eddies (Ridderinkhof et al., 2010). Northward flowing
119 bottom currents transporting North Atlantic Deep Water and Antarctic Intermediate Water masses are
120 found at depths below 2000 m (Collins et al., 2016). Annual mean velocities of the southward flow
121 decrease progressively in the upper 1500 m of the water column within the Mozambique Channel (de
122 Ruijter Wilhelmus. et al., 2002; Ullgren et al., 2012).

123 Based on the fact that the geomorphology of the Zambezi deep-sea fan evolved from lobated to
124 elongated during the Miocene, Walford et al. (2005) proposed that the strong southward Mozambique
125 Current was established in the early Miocene (~24 Ma). Before the early Miocene, there was no
126 “strong” influence of a north-south current on sediment distribution (Walford et al., 2005). Based on
127 detailed seismic stratigraphic analyses, a similar early Miocene onset age for the intensification of the
128 Mozambique Current is proposed by Preu et al. (2011). In contrast, several late Cretaceous current –
129 controlled deposits influenced by north – south current in the Mozambique Basin were associated with

130 the identification of late Cretaceous contourite deposits in the Somali Basin thus suggesting that a
131 southward coast-parallel current originating from or North of the Somali Basin flowed into and
132 through the Mozambique Channel in late Cretaceous times (Castelino et al., 2016, 2015).

133 2.3. Potential sources of sediments deposited in the Mozambique Channel

134 The Cenozoic fine-grained sediments deposited at DSDP 25 Site 242 are likely deposited by
135 southward and northward paleo-oceanic currents and originated from by rivers draining the African
136 continent and Madagascar. Southward paleo-oceanic current may have similar direction as the modern
137 Mozambique Current and hence transported sediments may have similar composition. As the NEMC
138 approaches the African coast entering the Mozambique Channel to feed into the Mozambique Current, it
139 may receive sediments from: 1) African rivers draining the Neoproterozoic Mozambique Belt and younger
140 volcanic and sedimentary deposits, 2) rivers of NW Madagascar that drain Paleozoic to Quaternary
141 sedimentary rocks and Cenozoic volcanic rocks and 3) volcanic rocks from the Comoros and Mayotte
142 island (van der Lubbe et al., 2016). A present-day surface sediment sampled close to the DSDP 25 Site 242
143 leg yields an $\epsilon_{Nd(0)}$ value of -11.2 (van der Lubbe et al., 2016, Fig. 1), and may be considered as
144 representative of sediments transported by the NEMC and deposited in the Mozambique Channel by the
145 Mozambique Current. Northward paleo-undercurrent may follow a reverse trajectory to that of the present-
146 day Agulhas Current (AC in Fig.1). Hence, sediments potentially transported by this near-bottom current
147 may receive detrital input from southeastern African rivers draining the Archean Zimbabwe craton, the
148 Mesoproterozoic Southern Irumide belt, Phanerozoic sedimentary rocks and volcanic deposits of the Karoo
149 supergroup. These sedimentary end-members might be best represented by the Limpopo and Zambezi
150 rivers (see Fig. 1A for localization), which are the largest single sediment contributors to the southwestern
151 Indian Ocean. In addition to these rivers, one possible endmember could be the Congo river as it might
152 have discharged into the Indian Ocean via the Rufiji Delta, located in Tanzania (northward the study area,
153 see Fig. 1A for location), prior to the uplift of the East African rift system during the Eocene-Oligocene
154 (Stankiewicz and de Wit, 2006). To constrain the Congo endmember, we calculated the mean $\epsilon_{Nd(0)}$ values
155 and Nd concentrations of the KZR-23 core sediments reported in Bayon et al. (2019). This gives a $\epsilon_{Nd(0)}$
156 value of -15.6 and Nd concentration of 23.5 ppm. To characterize the Limpopo and Zambezi river
157 sediments, volcanic rocks from the Comoros and Mayotte islands and sediments deposited on the

158 Mozambique margin, we have compiled 142 published Sr and Nd isotope data (supporting information
159 Table S1 (Deniel, 1998; Garzanti et al., 2014; Pelleter et al., 2014; Tucker et al., 1999; van der Lubbe et al.,
160 2016). Based on this compilation, there is a quite distinct average $\epsilon_{Nd(0)}$ values on modern sedimentary
161 input if considered samples are from the Limpopo (-26.2 Standard Deviation (S.D.4.3) and upstream
162 Zambezi (-12.4, S.D.: 4.0) river sediments, as well as from the Comoros (2.3, S.D.:1.5) and Mayotte (4.1,
163 S.D.:0.8) volcanic rocks. In comparison, modern Mozambique Channel sediments yield $\epsilon_{Nd(0)}$ values range
164 between -17.7 and -11.2 (mean value: -15.5, S.D.:1.5), which encompasses the average $\epsilon_{Nd(0)}$ value for
165 modern Zambezi shelf surface clay (-16.7; $1\sigma \pm 0.6$, $n=5$) and, hence, modern Zambezi suspension load
166 (van der Lubbe et al., 2016). This average value is lower than the $\epsilon_{Nd(0)}$ values of upstream Zambezi river
167 sediments measured by Garzanti et al (2014), thus indicating that the Zambezi suspended load also receives
168 contributions from old Zimbabwe and Mozambique belt cratonic terrains. Sediments from the Limpopo
169 (0.737850, S.D.: 0.024686) and Zambezi (0.7182750, S.D.: 0.010343) river sediments, and Comoros
170 (0.703538, S.D.: 0.000272) and Mayotte (0.703351, S.D.: 0.000130) volcanics also present distinct
171 $^{87}Sr/^{86}Sr$ isotopic compositions. The Archean Madagascar terranes have a mean $\epsilon_{Nd(0)}$ value and $^{87}Sr/^{86}Sr$
172 isotopic composition of -22.6 (S.D.:8.7) and 0.716081, (S.D.:0.014705), respectively (Table S1). Holocene
173 sediments deposited in a deep-sea interfluvial proximal to the mouths of major northwestern Madagascan
174 rivers yield a mean $\epsilon_{Nd(0)}$ of -19.5, S.D.: 0.3 (Table S1, Fontanier et al., 2018).

175 **Materials and Methods**

176 3.1 Sampling

177 Thirty-six pelagic and hemipelagic sediments were sampled from DSDP leg 25 Site 242 (Table 1).
178 The age of the samples has been determined based on nanoplankton zonation and planktonic foraminifera
179 determination (Simpson et al., 1974). The samples range from late Eocene to Quaternary (Table 1). Details
180 regarding the lithology, mineralogy and biostratigraphy of the analyzed samples can be found in the
181 Shipboard Scientific Party Site report (Simpson et al., 1974).

182

183 3.2 Major and trace elements and Sr-Nd isotopes

184 3.3.1 Sample preparation

185 Each bulk sample was gently crushed in an agate mortar. About 3 g of the crushed sediment
186 were placed into 50-ml centrifuge tubes for sequential leaching to remove the non-terrigenous
187 sedimentary components following the method of Bayon et al. (2002). Three different solutions
188 composed of 5% acetic acid, 15% acetic acid and hydroxylamine hydrochloride (0.05 M) and
189 hydrogen peroxide (H₂O₂, 5%) were then added to remove the carbonates, Fe-Mn oxides and organic
190 carbon, respectively. After the removal of non-terrigenous components, the residual fractions were
191 cleaned with ultrapure water (MQ-H₂O, 18 MΩ). Clayey (<2 μm) and silty (2-63 μm) fractions were
192 then separated by centrifugation in two steps. First, 25 ml of MQ-H₂O were added to the detrital
193 residues in the tubes, shaken vigorously, and then centrifuged for 2 min at 1000 rpm (133 g). The clay-
194 rich supernatants were immediately transferred into new 50 ml centrifuge tubes. Another 25 ml of
195 MQ-H₂O was added to silt-rich detrital residues, mixed thoroughly again, centrifuged for 2.5 min at
196 800 rpm (85 g), and transferred into corresponding centrifuge tubes. Finally, clay-size fractions were
197 collected after decantation (48 hours) and centrifugation at 3500 rpm (1630 g) from the residual
198 detrital material using low-speed centrifugation (Bayon et al., 2015). These clay-size fractions were
199 then analyzed for their major and trace element concentrations and their Sr-Nd isotopic compositions.

200 3.3.2 Major and trace element analyses

201 The major and trace element concentrations of the clay-size fractions were measured at the
202 Service d'Analyse des Roches et Minéraux (SARM, INSU facility, Vandoeuvre-Les-Nancy, France)
203 by ICP-OES (Na, Mg, K, Ca, Sc, Ti, Mn, Fe, Al, Si and P) and ICP-MS (Rb, Cs, Ba, Sr, Th, U, Y, Zr,
204 Nb, Hf, Cr, V, Co, Cu, Ni, Zn, La, Ce, Pr, Nd, Sm, Eu, Gd, Tb, Dy, Ho, Er, Tm, Yb, Lu and Ta) after
205 alkali fusion. Analytical details are available at <http://helium.crgp.cnrs-nancy.fr/SARM/> and in
206 Carignan et al. (2001). Uncertainties are lower than 5% for elements measured by ICP-OES, and lower
207 than 10% for elements measured by ICP-MS (see supplementary material Table S2).

209 Among the samples analyzed for Sr and Nd isotopes, twenty-one were analyzed at the
210 Geochronology Laboratory of the University of Brasília (Geochronos) and nine at the Geosciences
211 Environment Toulouse (GET) in France.

212 At GET, about 100 mg of the leached detrital residue fractions were accurately weighed into cleaned
213 Savillex PFA vials prior to digestion at elevated temperatures in the GET clean room. Organic matter
214 was first oxidized by hydrogen peroxide (H₂O₂) for 24 hours at ambient temperature, and then
215 digested in HNO₃ for 24 hours at 80°C followed by HF-HNO₃ for 24 hours at 80°C, and, finally
216 digested in HCl+HNO₃ for 24 hours at 115°C. Blank tests were performed to estimate the level of
217 contamination induced by the acid digestion, but it was found to be negligible. Aliquots containing
218 about 1000 ng of Sr and Nd were loaded into the ion exchange columns. Sr and Nd were separated
219 using the Sr-SPEC, TRU-SPEC and LN-SPEC resins Eichrom. Nd and Sr isotopic ratios were
220 measured using a Finnigan Mat 261 thermal ionization mass spectrometer and a Triton Thermal
221 Ionization Mass Spectrometer (TIMS) in dynamic mode. During the Nd runs, a ¹⁴⁶Nd/¹⁴⁴Nd ratio of
222 0.7219 was used to correct the signal for mass fractionation. For each sample, checks were made for
223 the absence of samarium (Sm). The accuracy of the measurements was estimated on the La Jolla
224 standard. Repeated analyses of the La Jolla standard gave a ¹⁴³Nd/¹⁴⁴Nd ratio of 0.511867 ± 0.000018
225 (2 S.D, n = 12) in agreement with the recommended value of 0.511858 (Lugmair et al., 1983). During
226 the Sr runs, ⁸⁶Sr/⁸⁸Sr = 0.1194 was used to correct the signal for mass fractionation. The accuracy of
227 the ⁸⁷Sr/⁸⁶Sr measurements was checked against the NBS 987 standard (= 0.710240) Hodell et al.,
228 2007). Repeated analyses of the NBS 987 standard gave an ⁸⁷Sr/⁸⁶Sr ratio of 0.710231 ± 0.000032
229 (2SD, n = 15) in agreement with the recommended value of Hodell et al. (2007) therefore no
230 instrumental bias needs to be taken into account. Total blanks (acid digestion plus column chemistry)
231 for Nd and Sr were checked by ICP-MS and found to be negligible (<1 per mil) compared to the Nd
232 and Sr amounts loaded onto the columns.

233 At the Geochronos Lab of the Geosciences Institute of the Universidade de Brasília, 20–40 mg
234 aliquots of the sediments were digested under clean laboratory conditions in two stages using
235 concentrated HF-HNO₃ and 6 N HCl on a hot plate. The Nd were separated using chromatographic
236 columns, including AG 50W-X8 cation exchange resin for Sr and Rare Earth Elements (REEs).
237 Neodymium was further isolated from the REE fraction using a second AG 50-X2 cation-exchange
238 resin. Neodymium was loaded on double rhenium filaments with H₃PO₄ (0.1 M) and measured as a
239 metal (Nd⁺) (Gioia and Pimentel, 2000). All of these analyses were performed on a TIMS
240 (ThermoFisher, Triton).

241 The measured ¹⁴³Nd/¹⁴⁴Nd_{sample} ratios are expressed in epsilon notation as the fractional
242 deviation in parts per 10⁴ (units) from ¹⁴³Nd/¹⁴⁴Nd value of in the Chondritic Uniform Reservoir
243 (CHUR). This notation is defined as: $\epsilon_{Nd}(t) = [(^{143}\text{Nd}/^{144}\text{Nd})_{\text{sample}(t)} / (^{143}\text{Nd}/^{144}\text{Nd})_{\text{CHUR}(t)} -$
244 $1] \times 10^4$

245 where t indicates the time at which ϵ_{Nd} is calculated. Here, no time correction is applied ($t = 0$)
246 and the $^{143}\text{Nd}/^{144}\text{Nd}_{\text{CHUR}(0)} = 0.512638$ (Jacobsen and Wasserburg, 1980).

247

248 **Results**

249 Major and trace element concentrations and Sr-Nd isotopic compositions of samples analyzed
250 in this study are reported in Table 2 and Table 3, respectively. Table 4 reports the mean values and
251 associated standard deviation of elemental ratios and isotopic composition for each age period.

252 4.1 Major elements, Large-Ion Lithophile Elements (LILE), High Field Strength Elements 253 (HFSE) and Trace Transition Elements (TTE)

254 The elemental concentrations of major elements, Large-Ion Lithophile Elements (LILE), High
255 Field Strength Elements (HFSE) and Trace Transition Elements (TTE) of samples normalized to the
256 Post Archean Australian Shales (PAAS) concentration are shown in Fig. 2. As a whole, the elemental
257 composition of the analyzed DSDP samples is rather uniform. They show depletions in SiO₂, MnO,

258 K₂O, Cs, Sr, U, Zr and Hf against PAAS, values which are representative of the upper continental crust
259 composition (Taylor and McLennan, 1985). Other elemental concentrations are close to PAAS values.
260 Four samples (3R3W, 6R3W, 14R3W, 17R1W) show slight enrichment in CaO and Sr against PAAS
261 that might be due to incomplete removal of marine carbonates. No apparent trend of major depletion or
262 enrichment in elemental concentration is recorded through time.

263 It might be possible to assess the degree of source-area weathering and subsequently paleo-
264 weathering conditions of ancient sediments using the Chemical Index of Alteration (CIA) (Nesbitt and
265 Young, 1982; Fedo et al., 1995) (Table 2). This index measures the weathering intensity of feldspars
266 relative to unaltered protoliths, and is defined as: $CIA = [Al_2O_3 / (Al_2O_3 + CaO^* + Na_2O + K_2O)] \times 100$ (in
267 molar proportions), where CaO* represents the CaO content in the silicate fraction. CIA values for
268 unaltered plagioclase and K-feldspars typical of unaltered upper crustal rocks are approximately equal
269 to 50, whereas higher CIA values represent higher degrees of weathering. For comparison, the CIA
270 value of the PAAS standard is equal to 67 (Taylor and McLennan, 1985).

271 As aforementioned, four samples enriched in CaO, probably due to incomplete removal of
272 marine carbonates, have anomalous low CIA values (between 44 and 64, Table 2). The remaining
273 DSDP samples yield higher CIA values (72 to 84). There is a slight increase in CIA values from the
274 late Eocene (mean $\sim 72 \pm 4$) to the late Oligocene (mean $\sim 78 \pm 1$). The CIA values from sample
275 younger than late Oligocene are comparable. The Al/Si atomic ratio of analyzed DSDP samples range
276 from 0.38 to 0.54 (Table 2). The analyzed DSDP site samples have slightly higher Cr/Th ratios (7.7 to
277 13.7) and lower Th/Sc ratios (0.50 to 0.74) than PAAS (Table 2). There is no apparent variation of the
278 Cr/Th ratios as a function of the age of the sample (Table 2). There is a slight decrease of the mean
279 Th/Sc ratio with the age.

280 4.2 Rare Earth Elements (REE)

281 The DSDP samples have comparable REE patterns with flat Light and Middle REE and
282 depletion in Heavy REE (HREE) against PAAS (Fig. 3). To facilitate comparisons with sediments
283 derived from basic or felsic sources (Cullers, 2000) and the PAAS (Taylor and McLennan, 1985), the
284 Eu anomaly is calculated with respect to chondrites: $Eu/Eu^* = Eu_N / (Sm_N \times Gd_N)^{1/2}$ where N refers to

285 the chondrite-normalized concentration value. The Eu/Eu* ratios of DSDP samples are slightly higher
286 (0.63-0.72) to that of the PAAS standard (*i.e.*, $\text{Eu/Eu}^* = 0.57 \pm 0.02$, Pourmand et al., 2012). There is a
287 slight increase of the mean Eu/Eu* ratio in DSDP samples from the late Eocene to the late Miocene
288 (Fig. 3). The Cerium anomaly (Ω_{Ce}) normalized to PAAS is calculated following De Baar et al.
289 (1985): $\Omega_{\text{Ce}} = 2 \times (\text{Ce}_{\text{sample}}/\text{Ce}_{\text{PAAS}}) / [(\text{La}_{\text{sample}}/\text{La}_{\text{PAAS}}) + (\text{Pr}_{\text{sample}}/\text{Pr}_{\text{PAAS}})]$, where
290 X_{sample} is the concentration of samples and X_{PAAS} refers to the concentrations of the PAAS standard
291 (Pourmand et al., 2012). The analyzed Ce anomalies display a narrow range of values (0.90-1.02)
292 close to the PAAS standard (*i.e.*, $\Omega_{\text{Ce}} = 1$).

293 4.3 Sr-Nd isotopes

294 Overall, the $^{87}\text{Sr}/^{86}\text{Sr}$ ratios of DSDP samples show a slight decrease from the late Eocene (mean ~
295 0.719626 ± 0.001305 , n=5) and the early Oligocene (mean ~ 0.72065 ± 0.004375 , n=6) to the Quaternary
296 (mean ~ 0.715576 ± 0.000685 , n=2). With the exception of one Quaternary sample (1R4W) and one late
297 Pliocene sample (2R3W), all DSDP samples show an overall decrease in $\epsilon_{\text{Nd}(0)}$ values from the late Eocene
298 to the Quaternary (from ~-14.1 to -11.8).

299 Discussion

300 5.1 Provenance of Cenozoic sediments

301 The REE contents, Eu anomalies, elemental ratios (Cr/Th and Th/Sc) and Sr-Nd isotopic
302 compositions of sedimentary rocks have been proven to be useful tools for determining the provenance
303 of sediments (McLennan et al., 1993). For instance, high Eu anomalies and Th/Sc and low Cr/Th are
304 characteristic of felsic and more highly differentiated source rocks, whereas high Cr/Th and low Eu
305 anomalies and Th/Sc suggest more mafic and less differentiated source rocks (Cullers, 2000;
306 McLennan et al., 1993). However, before drawing conclusions on provenance, the effects of chemical
307 weathering and marine authigenesis should be carefully assessed as these processes may control the
308 REE content and radiogenic isotope composition of marine sediments. The absence of any correlation
309 (*i.e.* $r \geq 0.75$) of CIA and Al/Si with REE content, Eu/Eu*, Cr/Th, Th/Sc, $^{87}\text{Sr}/^{86}\text{Sr}$ isotopic
310 compositions and $\epsilon_{\text{Nd}(0)}$ suggests that chemical weathering has not modified these provenance

311 proxies. Any influence from carbonates, Fe-Mn oxides or organic matter formed under marine
312 conditions should have been removed by the sequential carbonate dissolution and leaching steps.
313 Furthermore, all the analyzed DSDP samples have Ce anomalies higher than or equal to 0.90 and show
314 LREE enrichment and HREE depletions against PAAS. As the REE patterns of authigenic smectites
315 formed in deep-water environments are normally characterized by LREE depletion, HREE enrichment
316 and strong negative Ce anomalies ($\Omega_{Ce} < 0.50$, De Baar et al., 1985) typical of seawater (Piper, 1974),
317 this suggests that, even if authigenic smectites were incorporated during early diagenetic processes, its
318 proportion was much less than the detrital fraction.

319 Slight increase of Eu/Eu*, Cr/Th ratios, $\epsilon_{Nd(0)}$ values associated with slight decrease in Sr
320 isotopic composition and Th/Sc ratios from late Eocene to Quaternary point to slight input of more
321 “basic” sensu Cullers (2000), less differentiated and younger detritus to the DSDP 25 Site 242 and
322 DFZ through time (Figs 4 and 5). The late Eocene samples have the highest $\epsilon_{Nd(0)}$ values of the
323 analyzed samples (-14.1 ± 0.5 , n=4). They have $\epsilon_{Nd(0)}$ values significantly higher than those of
324 Madagascar Archean terranes (-22.6 ± 4.4 , n=15, Table S1, Tucker et al., 1999), Holocene sediments
325 deposited by major northwestern Madagascar rivers (-19.5 ± 0.2 , n=14, Table S1, (Fontanier et al.,
326 2018) and Limpopo River sediments (-26.2 ± 3.0 , n=8, Table S1, Garzanti et al., 2014), hence ruling
327 out Zimbabwe cratonic or Madagascar provenance as the main source of these sediments. In addition,
328 the late Eocene DSDP sediments have mean $\epsilon_{Nd(0)}$ values close to those which have been deposited at
329 1329 m water depth to the North of the Zambezi river during the past ~45,000 years ($\epsilon_{Nd(0)}$ -14.1 ± 0.2 ,
330 n = 52, Table S1, van der Lubbe et al. 2016) which may signify that they are sourced by paleo-rivers
331 that drained similar terranes. This may indicate they were drained by the paleo-Zambezi river
332 assuming that the late Eocene paleodrainage drained proportionally similar terranes as today.
333 Alternatively, the late Eocene sediments could have been sourced by the Paleo Congo river as it might
334 have discharged into the Indian Ocean prior to the uplift of the East African rift system during the
335 Eocene-Oligocene (Stankiewicz and de Wit, 2006). When compared with $\epsilon_{Nd(0)}$ values of the late
336 Eocene DSDP 25 site 242, Holocene muds of the Congo fan have $\epsilon_{Nd(0)}$ values slightly lower ($-15.6 \pm$
337 0.1 1 S.D.; (Bayon et al., 2019)) than those of the late Eocene-Oligocene. Three late Pliocene to

338 Quaternary samples out of five have $\epsilon_{Nd(0)}$ values similar to that of the northernmost present-day
339 surface sediments deposited on the Davie Ridge ($\epsilon_{Nd(0)} = -11.2$, van der Lubbe et al., 2016).
340 Furthermore, the late Eocene to early Oligocene samples have $\epsilon_{Nd(0)}$ values similar to those of the
341 Zambezi and present-day surface sediments situated west to the DFZ and DSDP 25 Site 242 (i.e. $\epsilon_{Nd(0)}$
342 $= -14.4$, van der Lubbe et al. 2016, Fig. 1). The high radiogenic $\epsilon_{Nd(0)}$ value of the lower part of the
343 DSDP core is interpreted to reflect mixing between low Nd radiogenic detritus originated from the
344 Paleo Zambezi or the Paleo Congo rivers and high radiogenic detritus coming from the north and
345 transported by the NEMC (van der Lubbe et al., 2016). Potential sources that could explain the
346 contribution of high radiogenic Nd detritus to the NEMC include 1) the Lurio and Rovuma Rivers that
347 drain the Neoproterozoic Mozambique Belt and geologically younger volcanic and sedimentary
348 deposits, and 2) Cenozoic volcanic rocks of the Comoros and Mayotte islands. At present, it is
349 impossible to further distinguish between these two potential sources, because there is no published Nd
350 isotopic compositions of sediments from Lurio and Rovuma to the best of our knowledge. Whatever
351 these contributors may be, we interpret the high radiogenic $\epsilon_{Nd(0)}$ values of the youngest Quaternary
352 DSDP sample (1R2W) analyzed in this study and the northernmost sediment deposited in the
353 Mozambique Channel analyzed by van der Lubbe et al. (2016) as representative of sediments
354 deposited by the NEMC before being mixed with Paleo Zambezi or Paleo Congo river detritus.
355 Together with the $\epsilon_{Nd(0)}$ values, Eu/Eu* and Cr/Th ratios also increase, whereas the $^{87}Sr/^{86}Sr$ and Th/Sc
356 ratios decrease from the late Eocene to the Quaternary (Figs 4 and 5). These trends may be interpreted
357 to reflect an increasing contribution of NEMC transported suspended material and/or lowering
358 contributions of Zambezi or Congo suspended load through time. In this scenario, using a simple
359 mixing equation (1), we can calculate the relative contribution of the Zambezi/Paleo Congo and
360 NEMC material in each sediment DSDP 25 site 242 sample.

361 Unfortunately, there is no Nd concentration available for the study of van der Lubbe et al.
362 (2016) to better constrain the NEMC and Paleo Zambezi/Paleo Congo (termed hereafter Southeast
363 Africa) endmembers. We assume that the NEMC Nd isotopic composition and concentration
364 endmember is represented by the youngest Quaternary sample (1R2W) analyzed in this study. To

365 constrain the Southeast Africa endmember, we used the Nd isotopic composition and concentration of
 366 the VM19-214 sample analyzed by Franzese et al. (2006), which represent the geochemical
 367 composition of sediments transported by the Mozambique Current after receiving the maximum input
 368 of Zambezi sediment. These end-members provide $\epsilon_{Nd(0)}$ values of -11.8 and -15.5 and Nd
 369 concentrations of 24.8 and 33.3 ppm for the NEMC and South Africa (SeA) endmembers, respectively.
 370 The relative contribution of South Africa (Zambezi/Congo) and NEMC endmembers can be calculated
 371 using the following equations:

$$372 \quad (\epsilon_{Nd(0)})_{DSDP} = (\epsilon_{Nd(0)})_{SeA} * X + (1 - X) \times (\epsilon_{Nd(0)})_{NEMC} \quad (1)$$

373 where X is the relative proportion of Nd delivered by the Southeast Africa (SeA) endmember
 374 in the sediment core sample.

$$375 \quad X = M_{SeA} \times C_{SeA} / M_{DSDP} \times C_{DSDP} \quad (2)$$

376 With M_{SeA} the sediment mass delivered by the Zambezi or Congo River, C_{SeA} the Nd
 377 concentration in the sediment of the Zambezi or Congo, M_{DSDP} the total sediment mass of the core
 378 sample and C_{DSDP} the Nd concentration in the core sample. Furthermore, we defined F_{SeA} as the mass
 379 fraction of the sediment in the core derived from the Zambezi or Congo rivers which is equal to the
 380 M_{SeA}/M_{DSDP} ratio. By combining the equations (1) and (2) we obtain the following equation:

$$381 \quad F_{SeA} = \frac{M_{SeA}}{M_{Core}} = \left((\epsilon_{Nd(0)})_{DSDP} - (\epsilon_{Nd(0)})_{NEMC} \right) \div \left((\epsilon_{Nd(0)})_{SeA} - (\epsilon_{Nd(0)})_{NEMC} \right) \times C_{DSDP}$$

$$382 \quad \div C_{SeA}$$

383 Using the Nd concentrations of analyzed sediments (Table 2), we can calculate the proportion
 384 of sediment originating from the Zambezi or Paleo Congo river in the Eocene-Oligocene DSDP
 385 sediments and originating from the Zambezi river in younger DSDP sediments. According to this
 386 calculation, there is an overall decrease of the Southeast African contribution from ~ 65.7% (Standard
 387 Deviation (S.D.) ~ 13.2) in the late Eocene to ~28.5% (S.D. ~ 10.0) in the early Pliocene. Additionally,
 388 there is a very strong variability in Southeast African contributions during the late Pliocene to
 389 Quaternary between virtually no contribution and up to 71.9% (Table 3 and Fig.5). These variations in
 390 the Southeast African contribution are not linear and roughly follow four steps. The oldest period

391 between the late Eocene and early Oligocene is characterized by Southeast African contribution \geq to
392 50%. The late Oligocene to early Miocene period shows general decrease in the Southeast African
393 contribution from \sim 37.4% to 51.2%. The third period between the middle Miocene and early Pliocene
394 has Southeast African contributions between \sim 23.4% and 28.5%. Finally, the youngest Pliocene-
395 Quaternary period shows strong variations between minor Southeast African contribution ($<5\%$) to
396 strong Southeast African contributions (52.8% and 71.9%).

397 5.2 Controls on provenance variations and implications for past oceanic circulation in the 398 Mozambique Channel

399 At present, the fine-grained sediments deposited at the location of DSDP 25 Site 242 are
400 expected to have very minor Zambezi contribution due to the combined presence of the Davie Ridge
401 and the strong southward Mozambique Current that may prevent Zambezi detritus reaching the DSDP
402 25 Site 242 location. In addition to variation in the Mozambique Current and tectonic activity of the
403 Davie Ridge, the variation in provenance and decrease in Zambezi contribution since the late Eocene
404 may be also caused by drainage change and variation in riverine supply in response to tectonic and
405 climatic change that may have affected Southeast Africa. Hence, the late Eocene to Quaternary
406 geochemical composition of DSDP 25 Site 242 sediments can be used as an archive of how the
407 variation of in riverine supply, drainage changes, tectonic activity of the Davie Ridge and variation in
408 the NEMC may have controlled their provenance (Fig.5).

409 The oldest period between the late Eocene and early Oligocene is characterized by the lowest
410 $\epsilon_{Nd(0)}$ values and strongest Southeast African contribution in the DSDP 25 site 242 samples. The onset
411 of the modern deltaic sedimentation in the Zambezi delta is thought to occur around the Eocene-
412 Oligocene boundary and is marked by Zambezi elevated sediment fluxes (Walford et al., 2005) and the
413 presence of a major tectonic controlled unconformity related to the second uplift phase of the South
414 African Plateau (Ponte et al., 2019). Before the late Eocene -early Oligocene (latest Bartonian to early
415 Priabonian, 38.2–36.2 Ma, Ponte et al. 2019), the Zambezi delta sediments recorded a stable tectonic
416 setting as emphasized by the presence of Eocene marine carbonates (Ponte et al., 2019). Given the

417 available stratigraphic resolution, it is unclear if the oldest samples analyzed here postdate or predate
418 this unconformity. If predating, the elevated Southeast African contribution and low $\epsilon_{Nd(0)}$ values
419 recorded by the DSDP 25 site 242 samples cannot be explained by the onset of modern sedimentation
420 in the Zambezi delta.

421 Alternatively, the late Eocene-early Oligocene sediments could have been sourced by a paleo-
422 river draining similar terranes as the Zambezi. One possible candidate could be the Paleo Congo river
423 which might have discharged into the Indian Ocean via the Rufiji Delta, located in Tanzania (see Fig.
424 1A), prior to the uplift of the East African rift system during the Eocene-Oligocene (Stankiewicz and
425 de Wit, 2006). In this scenario, the thick early Eocene-early Miocene slope and basin fan sedimentary
426 rocks (termed Mega-sequence 4) deposited over much of the Tanzania and Mozambique deepwater
427 offshore (McDonough et al., 2013) could represent the distal fan of the Paleo Congo river. This
428 scenario cannot be excluded on the basis of the $\epsilon_{Nd(0)}$ values of Congo river sediments which are
429 slightly lower (-15.6 ± 0.1 (1 S.D.); Bayon et al., (2019)) than those of the late Eocene-early
430 Oligocene. In this scenario, 100% of the sediment deposited at DSDP 25 Site 242 would be transported
431 by the NEMC and in turn this mean that the $\epsilon_{Nd(0)}$ values of sediment transported by the NEMC would
432 have changed between the early and late Oligocene. Then, the second uplift phase of the South African
433 Plateau (Baby et al., 2018) which coincides with the onset of modern sedimentation in the Zambezi
434 delta (Ponte et al., 2019) and elevated Zambezi sediment flux (Walford et al., 2005) might have
435 stopped the connection between the Paleo Congo and the Indian Ocean if it did exist.

436 Hence concerning the potential sources for the late Eocene-early Oligocene DSDP 25 site 242
437 samples, both a Zambezi and a Paleo Congo source are possible. If the Paleo Congo connection with
438 the Indian Ocean is stopped before the deposition of late Eocene-early Oligocene sediments, the low
439 $\epsilon_{Nd(0)}$ values of the DSDP 25 site 242 samples associated with low sedimentation rates at DSDP 25 Site
440 242 between the late Eocene and early Oligocene (3-9 m/m.y., (Simpson et al., 1974), Fig. 5) suggest
441 very minor contribution from a paleo southward NEMC. This could be due to the absence of tectonic
442 activity of the DFZ during the late Eocene –early Oligocene (Deville et al., 2018; Franke et al., 2015;
443 Mahanjane, 2014; Mougenot et al., 1986), which may not have acted as a barrier to sediments coming

444 from the South African coast to the DSDP 25 Site 242 or absence or low intensity of the NEMC which
445 may have not been capable of transporting detritus with higher $\epsilon_{Nd(0)}$ values.

446 The DFZ is thought to have experienced a southerly extension related to East African Rifting
447 System since the Oligocene (Deville et al., 2018; Franke et al., 2015; Mahanjane, 2014; Mougenot et
448 al., 1986). This extension coincides with a period of an elevated sediment flux during Oligocene times
449 (34–24 Ma) in the Zambezi deep-sea fan as a response of rapid regional uplift of Southern Africa
450 (Walford et al. 2005; Baby et al., 2018) that may explain the strong contribution of Southeast African
451 detritus to DSDP 25 Site 242 sediments. This is in agreement with the increase in mass accumulation
452 rate at DSDP 25 site 242 between the late Oligocene and middle Miocene (14 to 23 m/m.y., (Simpson
453 et al., 1974) when compared with those of the late Eocene-early Oligocene period (Fig. 5). In the
454 middle Miocene, graben formation in the DFZ possibly led to the abandonment of the NS Serpa Pinto
455 Valley and in turn to the export of Zambezi sediments to the Mozambique Channel through west-east
456 Zambezi Valley (Droz and Mougenot, 1987). This renewed tectonic activity in the DFZ may have
457 promoted the formation of a barrier preventing the arrival of Zambezi sediments to DSDP 25 Site 242
458 location, which would explain the decrease in Southeast African contribution between the early and
459 middle Miocene (from ~51 to ~23%). Alternatively, this reduction can also be explained by
460 strengthening of the southward flowing Mozambique Current. The initiation of the southward
461 Mozambique Current and its effect on sediment dispersion in the Mozambique Channel are
462 controverted. Recognition of late Cretaceous contourites deposits in the Somali Basin (Coffin et al.,
463 1986) associated with identification of late Cretaceous north to south current-controlled deposits in the
464 Mozambique Basin (Castelino et al., 2015) have been interpreted to document the existence of
465 southward coast-parallel current that was flowing into and through the Mozambique Channel in late
466 Cretaceous times (Castelino et al., 2015). In contrast, the morphology of the Zambezi deep-sea fan
467 changed from lobate to elongate during the Miocene, which suggests that, there is no “strong”
468 influence of a southward flowing current on sediment distribution in the Mozambique Channel before
469 the early Miocene (Walford et al. 2005). Rather, these authors proposed that the southward
470 Mozambique Current was established in the early Miocene (Walford et al., 2005). This early Miocene

471 age for the presence of the Mozambique Current is also confirmed by the identification of plastered
472 drift sequences south of the Mozambique Channel along the continental margin of Mozambique off the
473 Limpopo River (Preu et al., 2011). As there is no published evidence for change in drainage
474 configuration of the Zambezi catchment, we argue that the drop in Southeast African contribution
475 between the early and middle Miocene could be explained by a combination of uplift of the DFZ
476 and/or strengthening of the Mozambique Current.

477 The late Pliocene-Quaternary period is marked by a large spread in $\mathcal{E}_{Nd(0)}$ values and Southeast
478 African contribution in sediments deposited at DSDP 25 Site 242. Calculated sedimentary fluxes
479 exported by the Zambezi river to the Mozambique basin show a period of elevated flux from late
480 Miocene times (10 Ma) to present day due to a doubling of the size of the Zambezi catchment during
481 the Pliocene (Walford et al., 2005). This could explain the strong Southeast African contribution for
482 late Pliocene 2R3W and Quaternary 1R4W samples. However, it cannot explain the low Southeast
483 African contributions for other analyzed samples (Table 3 and Fig. 5). Alternatively, the low Southeast
484 African contribution for other late Pliocene-Quaternary sediments (Table 3) could be explained by
485 increasing tectonic activity of DFZ or increasing intensification of Mozambique Current. However,
486 these mechanisms cannot account for the strong Southeast African contribution in samples 2R3W and
487 1R4W. We propose therefore that the strong $\mathcal{E}_{Nd(0)}$ variations and in turn inferred Zambezi (Southeast
488 Africa) contributions during the late Pliocene-Quaternary are linked to the enhanced glacial-
489 interglacial cycles.

490 During sea-level highstand interglacial conditions, the accommodation space is increased in the
491 delta region which increased Zambezi sediment deposition in the delta and limited the amount of
492 Zambezi sediment delivered to the Mozambique Basin and Channel (Wiles et al., 2017). This also
493 result in higher Nd radiogenic isotopic composition of sediments (van der Lubbe et al., 2016)
494 deposited in the Mozambique Basin and Channel by the NEMC. The reverse is thought to occur during
495 glacial sea-level lowstand regression which promote bypassing of the shelf area and activation of deep-
496 sea canyons resulting in increasing delivery of Zambezi sediments to the Mozambique Basin and
497 Channel (Wiles et al., 2017) and lowering strength of the NEMC. These induced lower radiogenic Nd

498 isotopic composition of sediments (van der Lubbe et al., 2016) deposited in the Mozambique basin and
499 Channel. In this scenario, the late Pliocene 2R3W and Quaternary 1R4W would have been deposited
500 during glacial lowstands and other analyzed samples during interglacial highstand.

501 Our Nd isotopic data on DSDP 25 Site 242 supports an intensification of the Mozambique
502 Current from the late Pliocene and onwards, which prevented the arrival of Zambezi fine grained
503 sediments at DSDP 25 Site 242 during interglacial highstand and a combined effect of increasing
504 Zambezi sediment export to Mozambique Channel and Basin and lowering in the intensity of
505 Mozambique Current strength during glacial lowstand. Hence, these suggest that the dispersion of
506 fine-grained sediments within the Mozambique Channel is mainly controlled by strong glacial-
507 interglacial cycles and that it is no younger than late Pliocene.

508 **Conclusion**

509 The provenance study of late Eocene to Quaternary sediments deposited at the Davie Ridge
510 (Mozambique Channel) at DSDP 25 Site 242 shows that they contain a mixture of detritus originating
511 from the Zambezi or Congo river and transported from the North by the Mozambique Current. Based
512 on variations in Nd isotopic compositions and Nd concentrations, this study infers an overall decrease
513 of the Southeast African (Congo or Zambezi rivers) contribution from ~ 65.7% (S.D. ~ 13.2) in the late
514 Eocene to ~1.8% (S.D.~2.5) in the late Pliocene-Quaternary. This decrease in Southeast African
515 contributions roughly follows four steps. The oldest period between the late Eocene and early
516 Oligocene is characterized by Southeast African contribution (Congo or Zambezi rivers) close to or
517 superior to 50%. The late Oligocene- early Miocene period shows a first lowering of the Zambezi
518 contribution between ~ 37.4% and 51.2%. The third period between the middle Miocene and early
519 Pliocene has Zambezi contributions between ~23.4% and 28.5%. And finally the late Pliocene-
520 Quaternary period shows strong variations in Zambezi contribution (0 to 4.6% and 52.8-71.9%). The
521 causes for the low $\epsilon_{Nd(0)}$ values and high Southeast African contribution between the late Eocene and
522 the early Oligocene remain to be determined. It could record the onset of modern sedimentation in the
523 Zambezi delta or the discharge of the Paleo Congo river in the Indian Ocean. The overall lowering in
524 $\epsilon_{Nd(0)}$ values and Zambezi contribution between the late Oligocene and the early Pliocene is thought to

525 be due to the combined effect of increasing bathymetry of the Davie Ridge and onset and
526 intensification of the Mozambique Current. The strong variation in Zambezi contribution and $\epsilon_{Nd(0)}$
527 values in the late Pliocene-Quaternary is interpreted to be caused by glacial-interglacial cycles with
528 glacial lowstand favoring higher Zambezi contribution and lower $\epsilon_{Nd(0)}$ values and interglacial
529 highstand promoting lower Zambezi contribution and higher $\epsilon_{Nd(0)}$ values. Hence, these suggest that
530 the modern dispersion pattern of fine-grained sediments within the Mozambique Channel is no
531 younger than the late Pliocene.

532

533 **Acknowledgments**

534 This study was supported by the Actions Marges projects “Traçages des sources de la marge du nord
535 ouest de l’Afrique” and « Quantification et modélisation des transferts continent-océan aux différentes
536 échelles de temps (actuel-100Ma) exemple de la marge ouest de l’Afrique » funded by INSU-CNRS,
537 TOTAL, IFREMER and BRGM. This work used samples provided by the Deep Sea Drilling Project
538 (DSDP), which is sponsored by the US National Science Foundation and participating countries under
539 the management of the Joint Oceanographic Institutions (JOI), Inc. We also would like to thank Tristan
540 Rousseau and Yannick Murlot for having leached some of the DSDP samples when they were at
541 GET. We would like to thank the editor and two anonymous reviewers for their comments that helped
542 us to greatly improve this manuscript.

543

544 **References**

545 Baby, G., Guillocheau, F., Boulogne, C., Robin, C., Dall’Asta, M., 2018. Uplift history of a
546 transform continental margin revealed by the stratigraphic record: The case of the Agulhas transform
547 margin along the Southern African Plateau. *Tectonophysics* 731–732, 104–130.
548 <https://doi.org/10.1016/j.tecto.2018.03.014>

549 Bayon, G., German, C.R., Boella, R.M., Milton, J.A., Taylor, R.N., Nesbitt, R.W., 2002. An
550 improved method for extracting marine sediment fractions and its application to Sr and Nd isotopic
551 analysis. *Chem. Geol.* 187, 179–199. [https://doi.org/10.1016/S0009-541\(01\)00416-8](https://doi.org/10.1016/S0009-541(01)00416-8)

552 Bayon, G., Schefuß, E., Dupont, L., Borges, A.V., Dennielou, B., Lambert, T., Mollenhauer,
553 G., Monin, L., Ponzevera, E., Skonieczny, C., André, L., 2019. The roles of climate and human land-
554 use in the late Holocene rainforest crisis of Central Africa. *Earth Planet. Sci. Lett.* 505, 30–41.
555 <https://doi.org/10.1016/j.epsl.2018.10.016>

556 Bayon, G., Toucanne, S., Skonieczny, C., André, L., Bermell, S., Cheron, S., Dennielou, B.,
557 Etoubleau, J., Freslon, N., Gauchery, T., Germain, Y., Jorry, S.J., Ménot, G., Monin, L., Ponzevera, E.,
558 Rouget, M.-L., Tachikawa, K., Barrat, J.A., 2015. Rare earth elements and neodymium isotopes in
559 world river sediments revisited. *Geochim. Cosmochim. Acta* 170, 17–38.
560 <https://doi.org/10.1016/j.gca.2015.08.001>

561 Bonneau, L., Toucanne, S., Bayon, G., Jorry, S.J., Emmanuel, L., Silva Jacinto, R., 2017.
562 Glacial erosion dynamics in a small mountainous watershed (Southern French Alps): A source-to-
563 sink approach. *Earth Planet. Sci. Lett.* 458, 366–379.
564 <https://doi.org/10.1016/j.epsl.2016.11.004>

565 Castelino, J.A., Reichert, C., Klingelhoefer, F., Aslanian, D., Jokat, W., 2015. Mesozoic and
566 Early Cenozoic sediment influx and morphology of the Mozambique Basin. *Mar. Pet. Geol.* 66, 890–
567 905. <https://doi.org/10.1016/j.marpetgeo.2015.07.028>

568 Castelino, J.A., Eagles, G., Jokat, W., 2016. Anomalous bathymetry and palaeobathymetric
569 models of the Mozambique Basin and Riiser Larsen Sea. *Earth Planet. Sci. Lett.* 455, 25–37.
570 <https://doi.org/10.1016/j.epsl.2016.09.018>

571 Coffin, M.F., Rabinowitz, P.D., Houtz, R.E., 1986. Crustal structure in the Western Somali
572 Basin. *Geophys. J. Int.* 86, 331–369. <https://doi.org/10.1111/j.1365-246X.1986.tb03832.x>

573 Collins, C., Hermes, J.C., Roman, R.E., Reason, C.J.C., 2016. First dedicated hydrographic
574 survey of the Comoros Basin. *J. Geophys. Res. Oceans* 121, 1291–1305.
575 <https://doi.org/10.1002/2015JC011418>

576 Cullers, R.L., 2000. The geochemistry of shales, siltstones and sandstones of Pennsylvanian
577 Permian age, Colorado, USA: implications for provenance and metamorphic studies. *Lithos* 51, 181–
578 203. [https://doi.org/10.1016/S0024-4937\(99\)00063-8](https://doi.org/10.1016/S0024-4937(99)00063-8)

579 De Baar, H.J.W., Bacon, M.P., Brewer, P.G., Bruland, K.W., 1985. Rare earth elements in the
580 Pacific and Atlantic Oceans. *Geochim. Cosmochim. Acta* 49, 1943–1959.
581 [https://doi.org/10.1016/0016-7037\(85\)90089-4](https://doi.org/10.1016/0016-7037(85)90089-4)

582 de Ruijter Wilhelmus P. M., Ridderinkhof Herman, Lutjeharms Johann R. E., Schouten Mathijs
583 W., Veth Cornelis, 2002. Observations of the flow in the Mozambique Channel. *Geophys. Res. Lett.*
584 29, 140–1. <https://doi.org/10.1029/2001GL013714>

585 Deniel, C., 1998. Geochemical and isotopic (Sr, Nd, Pb) evidence for plume–lithosphere
586 interactions in the genesis of Grande Comore magmas (Indian Ocean). *Chem. Geol.* 144, 281–303.
587 [https://doi.org/10.1016/S0009-2541\(97\)00139-3](https://doi.org/10.1016/S0009-2541(97)00139-3)

588 Deville, E., Marsset, T., Courgeon, S., Jatiault, R., Ponte, J.-P., Thereau, E., Jouet, G., Jorry,
589 S.J., Droz, L., 2018. Active fault system across the oceanic lithosphere of the Mozambique Channel:
590 Implications for the Nubia–Somalia southern plate boundary. *Earth Planet. Sci. Lett.* 502, 210–220.
591 <https://doi.org/10.1016/j.epsl.2018.08.052>

592 Dia, A., Dupré, B., Allègre, C.J., 1992. Nd isotopes in Indian Ocean sediments used as a tracer
593 of supply to the ocean and circulation paths. *Mar. Geol.* 103, 349–359. [https://doi.org/10.1016/0025-](https://doi.org/10.1016/0025-3227(92)90025-D)
594 [3227\(92\)90025-D](https://doi.org/10.1016/0025-3227(92)90025-D)

595 Droz, L., Mougnot, D., 1987. Mozambique Upper Fan: Origin of Depositional Units. *AAPG*
596 *Bull.* 71, 1355–1365.

597 Fagel, N., Debrabant, P., André, L., 1994. Clay supplies in the Central Indian Basin since the
598 Late Miocene: climatic or tectonic control? *Mar. Geol.* 122, 151–172.
599 [https://doi.org/10.1016/0025-3227\(94\)90209-7](https://doi.org/10.1016/0025-3227(94)90209-7)

600 Fagel, N., Innocent, C., Stevenson, R.K., Hillaire-Marcel, C., 1999. Deep circulation changes
601 in the Labrador Sea since the Last Glacial Maximum: New constraints from Sm-Nd data on sediments.
602 *Paleoceanography* 14, 777–788. <https://doi.org/10.1029/1999PA900041>

603 Fontanier, C., Mamo, B., Toucanne, S., Bayon, G., Schmidt, S., Deflandre, B., Dennielou, B.,
604 Jouet, G., Garnier, E., Sakai, S., Lamas, R.M., Duros, P., Toyofuku, T., Salé, A., Belleney, D., Bichon,
605 S., Boissier, A., Chéron, S., Pitel, M., Roubi, A., Rovere, M., Grémare, A., Dupré, S., Jorry, S.J., 2018.
606 Are deep-sea ecosystems surrounding Madagascar threatened by land-use or climate change? Deep
607 Sea Res. Part Oceanogr. Res. Pap. 131, 93–100. <https://doi.org/10.1016/j.dsr.2017.11.011>

608 Franke, D., Jokat, W., Ladage, S., Stollhofen, H., Klimke, J., Lutz, R., Mahanjane, E.S.,
609 Ehrhardt, A., Schreckenberger, B., 2015. The offshore East African Rift System: Structural framework
610 at the toe of a juvenile rift. *Tectonics* 34, 2086–2104. <https://doi.org/10.1002/2015TC003922>

611 Franzese, A.M., Hemming, S.R., Goldstein, S.L., Anderson, R.F., 2006. Reduced Agulhas
612 Leakage during the Last Glacial Maximum inferred from an integrated provenance and flux study.
613 *Earth Planet. Sci. Lett.* 250, 72–88. <https://doi.org/10.1016/j.epsl.2006.07.002>

614 Garzanti, E., Padoan, M., Setti, M., López-Galindo, A., Villa, I.M., 2014. Provenance versus
615 weathering control on the composition of tropical river mud (southern Africa). *Chem. Geol.* 366, 61–
616 74. <https://doi.org/10.1016/j.chemgeo.2013.12.016>

617 Gioia, S.M.C.L., Pimentel, M.M., 2000. The Sm-Nd isotopic method in the geochronology
618 laboratory of the University of Brasília. *An. Acad. Bras. Ciênc.* 72, 219–245.
619 <https://doi.org/10.1590/S0001-37652000000200009>

620 Goldstein, S.L., O’Nions, R.K., 1981. Nd and Sr isotopic relationships in pelagic clays and
621 ferromanganese deposits. *Nature* 292, 324–327. <https://doi.org/10.1038/292324a0>

622 Grousset, F.E., Biscaye, P.E., Zindler, A., Prospero, J., Chester, R., 1988. Neodymium isotopes
623 as tracers in marine sediments and aerosols: North Atlantic. *Earth Planet. Sci. Lett.* 87, 367–378.
624 [https://doi.org/10.1016/0012-821X\(88\)90001-5](https://doi.org/10.1016/0012-821X(88)90001-5)

625 Grousset, F.E., Henry, F., Minster, J.F., Monaco, A., 1990. Nd isotopes as tracers in water
626 column particles: the western Mediterranean Sea. *Mar. Chem.* 30, 389–407.
627 [https://doi.org/10.1016/0304-4203\(90\)90083-O](https://doi.org/10.1016/0304-4203(90)90083-O)

628 Hodell, D.A., Kamenov, G.D., Hathorne, E.C., Zachos, J.C., Röhl, U., Westerhold, T., 2007.
629 Variations in the strontium isotope composition of seawater during the Paleocene and early Eocene

630 from ODP Leg 208 (Walvis Ridge). *Geochem. Geophys. Geosystems* 8.
631 <https://doi.org/10.1029/2007GC001607>

632 Innocent, C., Fagel, N., Stevenson, R.K., Hillaire-Marcel, C., 1997. Sm • Nd signature of
633 modern and late Quaternary sediments from the northwest North Atlantic: Implications for deep
634 current changes since the Last Glacial Maximum. *Earth Planet. Sci. Lett.* 146, 607–625.
635 [https://doi.org/10.1016/S0012-821X\(96\)00251-8](https://doi.org/10.1016/S0012-821X(96)00251-8)

636 Jacobsen, S.B., Wasserburg, G.J., 1980. Sm-Nd isotopic evolution of chondrites. *Earth Planet.*
637 *Sci. Lett.* 50, 139–155. [https://doi.org/10.1016/0012-821X\(80\)90125-9](https://doi.org/10.1016/0012-821X(80)90125-9)

638 Kolla, V., KostECKI, J.A., Henderson, L., Hess, L., 1980. Morphology and Quaternary
639 sedimentation of the Mozambique Fan and environs, southwestern Indian Oceans*. *Sedimentology* 27,
640 357–378. <https://doi.org/10.1111/j.1365-3091.1980.tb01188.x>

641 Liu, C., Clift, P.D., Carter, A., Böning, P., Hu, Z., Sun, Z., Pahnke, K., 2017. Controls on
642 modern erosion and the development of the Pearl River drainage in the late Paleogene. *Mar. Geol.,*
643 *Evolution of the Deep South China Sea: Integrated IODP Expedition 349 Results* 394, 52–68.
644 <https://doi.org/10.1016/j.margeo.2017.07.011>

645 Lugmair, G.W., Shimamura, T., Lewis, R.S., Anders, E., 1983. Samarium-146 in the Early
646 Solar System: Evidence from Neodymium in the Allende Meteorite. *Science* 222, 1015–1018.
647 <https://doi.org/10.1126/science.222.4627.1015>

648 Mahanjane, E.S., 2014. The Davie Fracture Zone and adjacent basins in the offshore
649 Mozambique Margin – A new insights for the hydrocarbon potential. *Mar. Pet. Geol.* 57, 561–571.
650 <https://doi.org/10.1016/j.marpetgeo.2014.06.015>

651 McDonough, K.-J., Bouanga, E., Pierard, C., Horn, B., Emmet, P., Gross, J., Danforth, A.,
652 Sterne, N., Granath, J., 2013. Wheeler-transformed 2D seismic data yield fan chronostratigraphy of
653 offshore Tanzania. *Lead. Edge* 32, 162–170. <https://doi.org/10.1190/tle32020162.1>

654 McLennan, S.M., Hemming, S., McDaniel, D.K., Hanson, G.N., 1993. Geochemical
655 approaches to sedimentation, provenance, and tectonics, in: *Geological Society of America Special*
656 *Papers*. Geological Society of America, pp. 21–40. <https://doi.org/10.1130/SPE284-p21>

657 Mougénot, D., Recq, M., Virlogeux, P., Lepvrier, C., 1986. Seaward Extension of the East-
658 African Rift. *Nature* 321, 599–603. <https://doi.org/10.1038/321599a0>

659 Murlot, Y., Roddaz, M., Dera, G., Calvès, G., Kim, J., Chaboureaud, A., Mounic, S., Raison,
660 F., 2018. Geochemical Evidence for Large-Scale Drainage Reorganization in Northwest Africa During
661 the Cretaceous. *Geochem. Geophys. Geosystems* 0. <https://doi.org/10.1029/2018GC007448>

662 Pelleter, A.-A., Caroff, M., Cordier, C., Bachelery, P., Nehlig, P., Debeuf, D., Arnaud, N.,
663 2014. Melilite-bearing lavas in Mayotte (France): An insight into the mantle source below the
664 Comores. *Lithos* 208–209, 281–297. <https://doi.org/10.1016/j.lithos.2014.09.012>

665 Piper, D.Z., 1974. Rare earth elements in ferromanganese nodules and other marine
666 phases. *Geochim. Cosmochim. Acta* 38, 1007–1022. [https://doi.org/10.1016/0016-](https://doi.org/10.1016/0016-7037(74)90002-7)
667 [7037\(74\)90002-7](https://doi.org/10.1016/0016-7037(74)90002-7)

668 Ponte, J.-P., Robin, C., Guillocheau, F., Popescu, S., Suc, J.-P., Dall’Asta, M., Melinte-
669 Dobrinescu, M.C., Bubik, M., Dupont, G., Gaillot, J., 2019. The Zambezi delta (Mozambique channel,
670 East Africa): High resolution dating combining bio- orbital and seismic stratigraphies to determine
671 climate (palaeoprecipitation) and tectonic controls on a passive margin. *Mar. Pet. Geol.* 105, 293–312.
672 <https://doi.org/10.1016/j.marpetgeo.2018.07.017>

673 Pourmand, A., Dauphas, N., Ireland, T.J., 2012. A novel extraction chromatography and MC-
674 ICP-MS technique for rapid analysis of REE, Sc and Y: Revising CI-chondrite and Post-Archean
675 Australian Shale (PAAS) abundances. *Chem. Geol.* 291, 38–54.
676 <https://doi.org/10.1016/j.chemgeo.2011.08.011>

677 Preu, B., Spieß, V., Schwenk, T., Schneider, R., 2011. Evidence for current-controlled
678 sedimentation along the southern Mozambique continental margin since Early Miocene times. *Geo-*
679 *Mar. Lett.* 31, 427–435. <https://doi.org/10.1007/s00367-011-0238-y>

680 Revel, M., Sinko, J.A., Grousset, F.E., Biscaye, P.E., 1996. Sr and Nd isotopes as tracers of
681 North Atlantic lithic particles: Paleoclimatic implications. *Paleoceanography* 11, 95–113.
682 <https://doi.org/10.1029/95PA03199>

683 Revel, M., Cremer, M., Grousset, F.E., Labeyrie, L., 1996. Grain-size and Sr-Nd isotopes as
684 tracer of paleo-bottom current strength, Northeast Atlantic Ocean. *Mar. Geol.* 131, 233–249.
685 [https://doi.org/10.1016/0025-3227\(96\)00005-9](https://doi.org/10.1016/0025-3227(96)00005-9)

686 Ridderinkhof, H., van der Werf, P.M., Ullgren, J.E., van Aken, H.M., van Leeuwen, P.J., de
687 Ruijter, W.P.M., 2010. Seasonal and interannual variability in the Mozambique Channel from moored
688 current observations. *J. Geophys. Res.* 115. <https://doi.org/10.1029/2009JC005619>

689 Simpson, E.S.W., Schlich, R., et al., 1974. Initial Reports of the Deep Sea Drilling Project, 25,
690 Initial Reports of the Deep Sea Drilling Project. U.S. Government Printing Office.
691 <https://doi.org/10.2973/dsdp.proc.25.1974>

692 Stankiewicz, J., de Wit, M.J., 2006. A proposed drainage evolution model for Central Africa—
693 Did the Congo flow east? *J. Afr. Earth Sci.* 44, 75–84. <https://doi.org/10.1016/j.jafrearsci.2005.11.008>

694 Taylor, S.R., McLennan, S.M., 1985. The continental crust: Its composition and evolution.

695 Tucker, R.D., Ashwal, L.D., Handke, M.J., Hamilton, M.A., Le Grange, M., Rabeloson,
696 R.A., 1999. U-Pb Geochronology and Isotope Geochemistry of the Archean and Proterozoic Rocks of
697 North-Central Madagascar. *J. Geol.* 107, 135–153. <https://doi.org/10.1086/314337>

698 Ullgren, J.E., van Aken, H.M., Ridderinkhof, H., de Ruijter, W.P.M., 2012. The hydrography
699 of the Mozambique Channel from six years of continuous temperature, salinity, and velocity
700 observations. *Deep Sea Res. Part Oceanogr. Res. Pap.* 69, 36–50.
701 <https://doi.org/10.1016/j.dsr.2012.07.003>

702 van der Lubbe, J. (H.) J. L., Frank, M., Tjallingii, R., Schneider, R.R., 2016. Neodymium
703 isotope constraints on provenance, dispersal, and climate-driven supply of Zambezi sediments along
704 the Mozambique Margin during the past ~45,000 years. *Geochem. Geophys. Geosystems* 17, 181–
705 198. <https://doi.org/10.1002/2015GC006080>

706 van der Lubbe, J. (H.) J. L., Tjallingii, R., Prins, M.A., Brummer, G.-J.A., Jung, S.J.A., Kroon,
707 D., Schneider, R.R., 2014. Sedimentation patterns off the Zambezi River over the last 20,000years.
708 *Mar. Geol.* 355, 189–201. <https://doi.org/10.1016/j.margeo.2014.05.012>

709 Walford, H.L., White, N.J., Sydow, J.C., 2005. Solid sediment load history of the Zambezi
710 Delta. *Earth Planet. Sci. Lett.* 238, 49–63. <https://doi.org/10.1016/j.epsl.2005.07.014>

711 **Figure captions**

712 **Figure 1.** A) Map of southeast Africa showing the main surface currents (solid thin arrows) in the
713 southwest Indian Ocean (adapted from van der Lubbe et al., 2016, 2014). The Zambezi and Limpopo
714 drainage basins are indicated by the grey shaded area. The location of the present-day delta of the Rufiji
715 River is also indicated because it might represent the embouchure of the paleo-Congo River (see text for
716 details). The South Equatorial Current (SEC) is the main source of water in the Madagascar region. It
717 bifurcates into the North East Madagascar Current (NEMC) and the South East Madagascar Current
718 (SEMC) where approaching Madagascar coast. Part of the NEMC waters enter the Mozambique Channel
719 (Ridderinkhof et al., 2010) and are responsible for the net southward flow through the Mozambique
720 Channel (MC). The flow through the Mozambique Channel occurs through the passage of large
721 anticyclonic eddies (Ridderinkhof et al., 2010). Sediments are mainly transported in southward direction
722 and deposited onto the large Mozambique deep-sea fan indicated in light gray (Kolla et al., 1980). The flow
723 through the Mozambique Channel is a source of the Agulhas Current (AC). The dashed rectangle indicates
724 the location of Fig. 1B. B) Detailed map of study area which shows the location of DSDP 25 Site 242 and
725 the surface distribution of selected previous published $\epsilon_{Nd(0)}$ values in clay-sized lithogenic surface
726 sediments in the Mozambique Channel (Franzese et al., 2006; van der Lubbe et al., 2016). The Zambezi
727 Catchment is indicated by the dark shaded area. Depth contours are drawn at 500 m. S.P.V.: Serpa Pinto
728 Valley

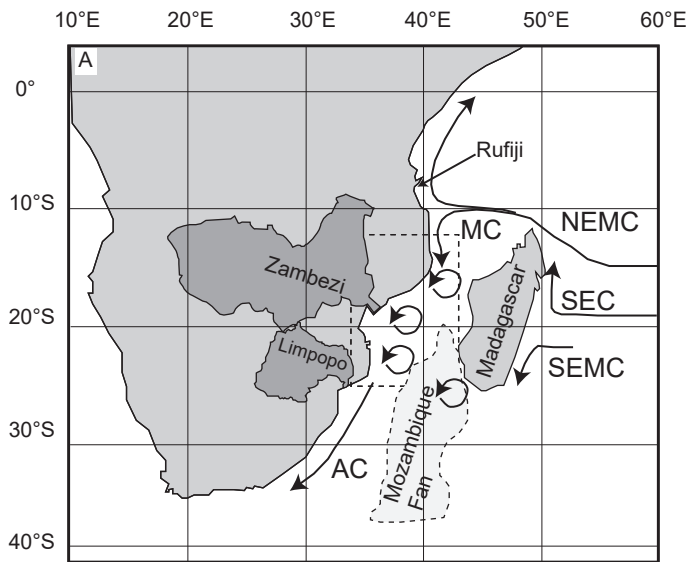
729 **Figure 2.** Major and selected trace element contents normalized to PAAS (Taylor and McLennan, 1985;
730 Pourmand et al., 2012). From left to right on the diagram, the major elements (SiO_2 , TiO_2 , Al_2O_3 , Fe_2O_3 ,
731 MnO , MgO , CaO , Na_2O , K_2O and P_2O_5), LILE (Rb, Cs, Ba, Sr, Th and U), HFSE (Y, Zr, Nb, Hf), and
732 TTE (Sc, Cr, Co, V and Ni) are plotted for DSDP 25 Site 242 samples.

733 **Figure 3.** Rare earth element (REE) contents normalized to PAAS (Taylor and McLennan, 1985;
734 Pourmand et al., 2012) for DSDP 25 Site 242 samples.

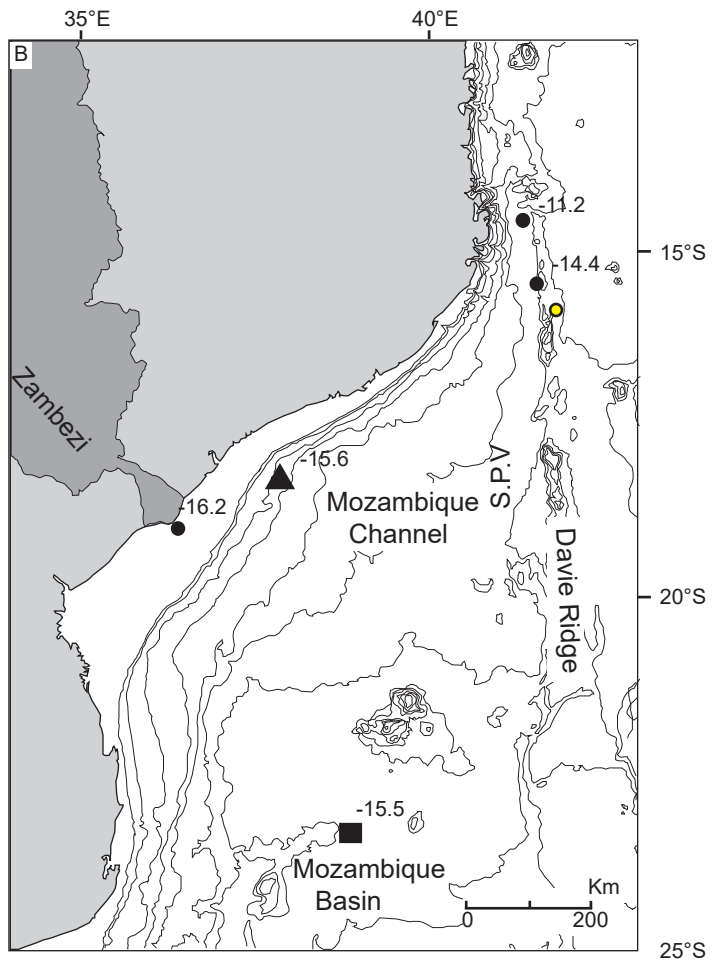
735 **Figure 4.** Variations of selected trace element ratios (Cr/Th, Th/Sc and Eu/Eu*, see text for details) since
736 the Eocene. The lengths of the horizontal bar for the Cr/Th, Th/Sc, and Eu/Eu*, correspond to 15% (the
737 sum of the Cr and Th concentration analytical errors), 25% (the sum of the Th and Sc concentration
738 analytical errors) and 5% (the Eu concentration analytical error, see supplementary material Table S2).
739 The main events with their duration affecting the studied area are also indicated. References are as follow:
740 (1) Walford et al. (2005), (2) Droz and Mougnot (1987), (3) Mahanjane (2014), (4) Baby et al. (2018).

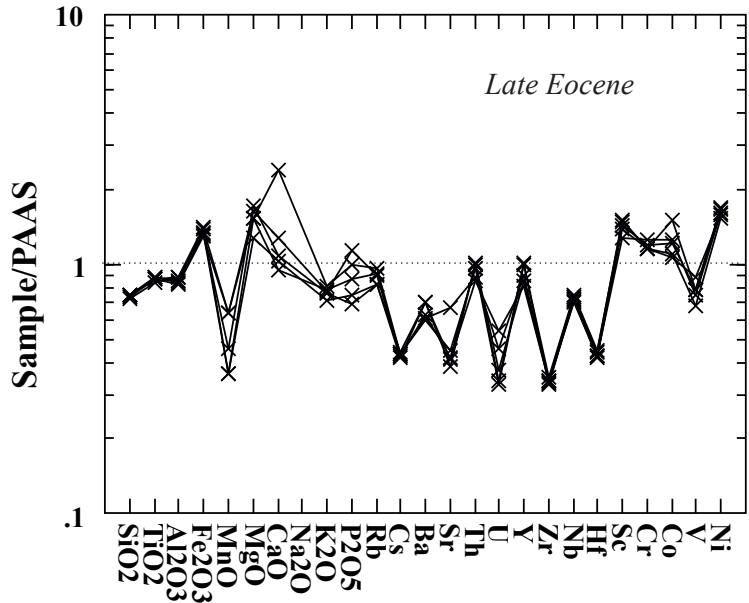
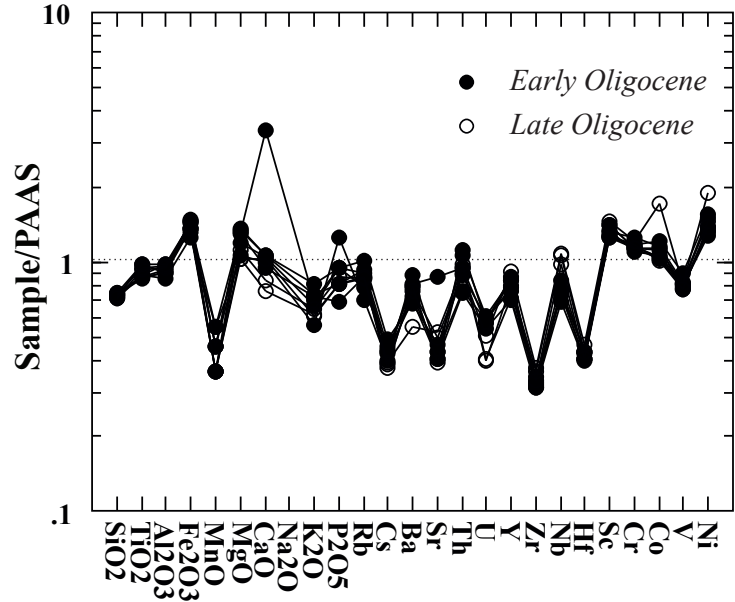
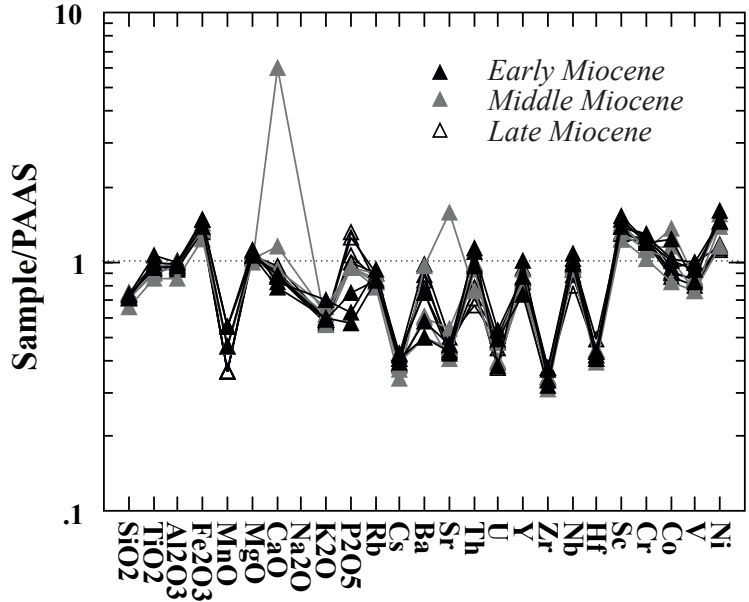
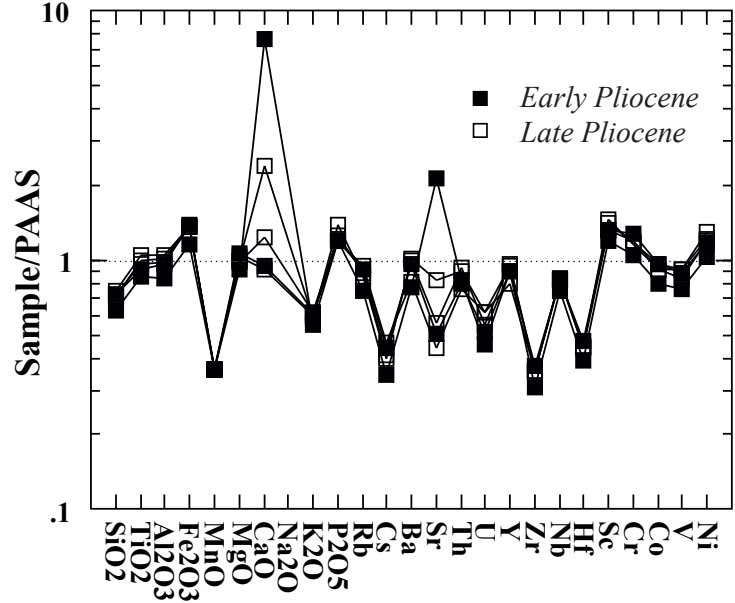
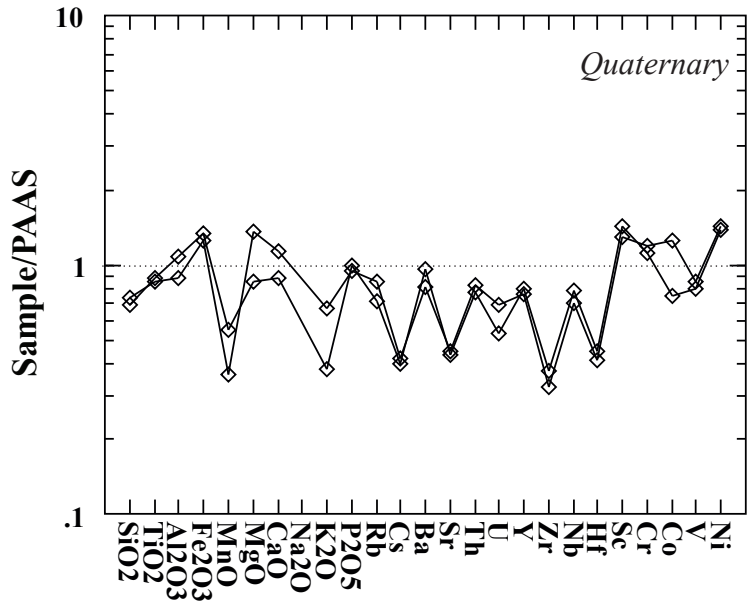
741 **Figure 5.** Variations of $^{87}\text{Sr}/^{86}\text{Sr}$ isotopic compositions, Nd isotopic compositions expressed as $\epsilon_{\text{Nd}(0)}$ values
742 and of Southeast African contributions in % (see text for details) since the Eocene. The lengths of the
743 horizontal bar for the Sr-Nd isotopic compositions correspond to 2σ analytical errors (see Table 3). The
744 lengths of the horizontal bar for the Southeast contribution correspond to the sum of the Nd concentration
745 analytical error (i.e 15%, see supplementary material Table S2) plus the % of the Nd isotopic composition
746 2σ analytical errors with respect to the measured Nd isotopic composition (see Table 3). The main events
747 with their duration affecting the studied area are also indicated. References are as follow: (1) Walford et al.
748 (2005), (2) Droz and Mougnot (1987), (3) Mahanjane (2014), (4) Baby et al. (2018). The sedimentation
749 rates are taken from Simpson et al. (1974) and expressed in m/m.y.

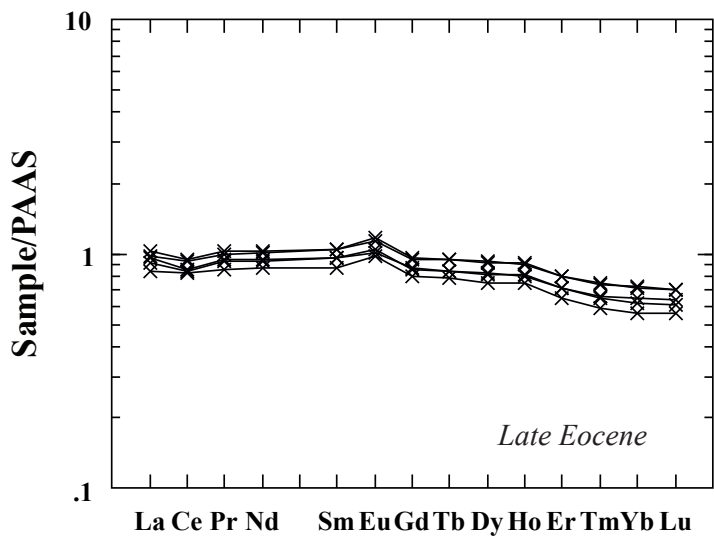
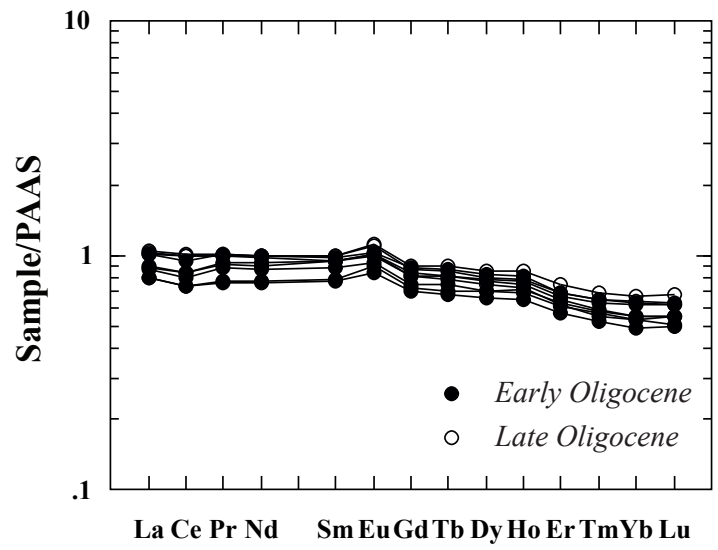
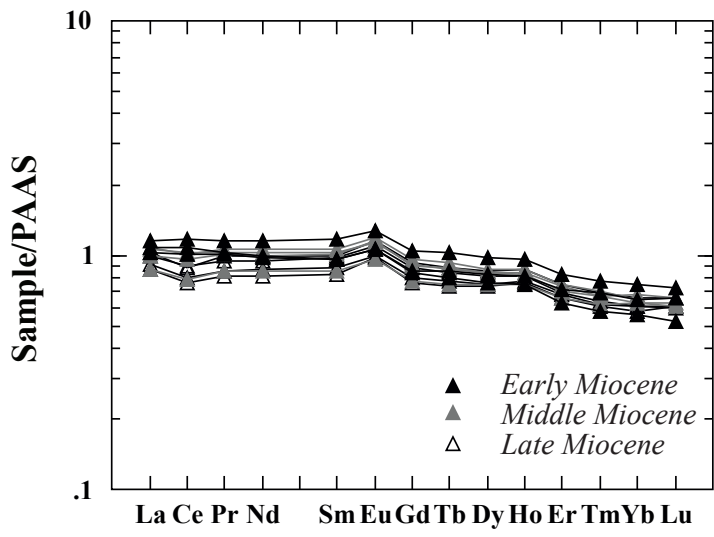
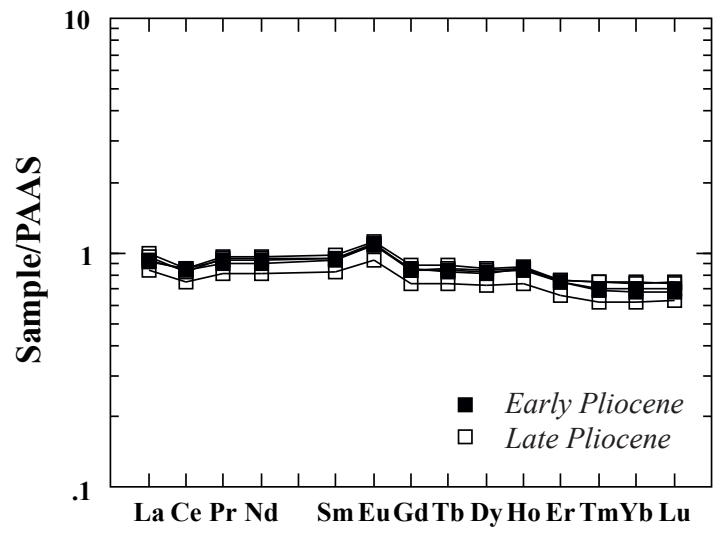
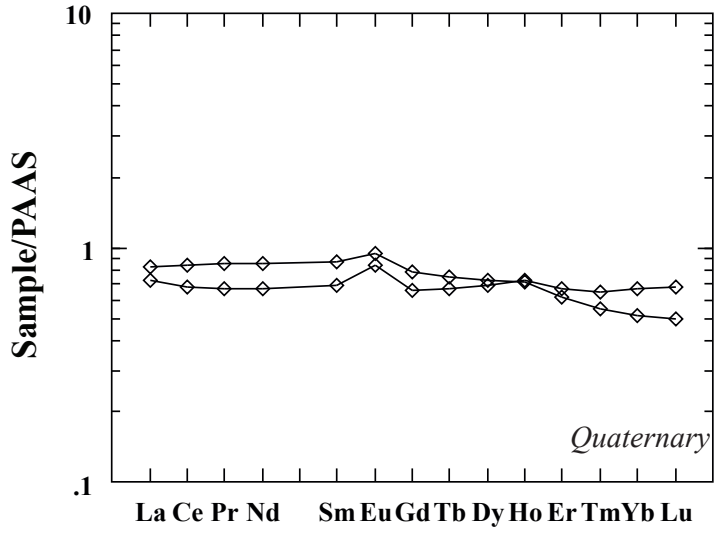
750
751

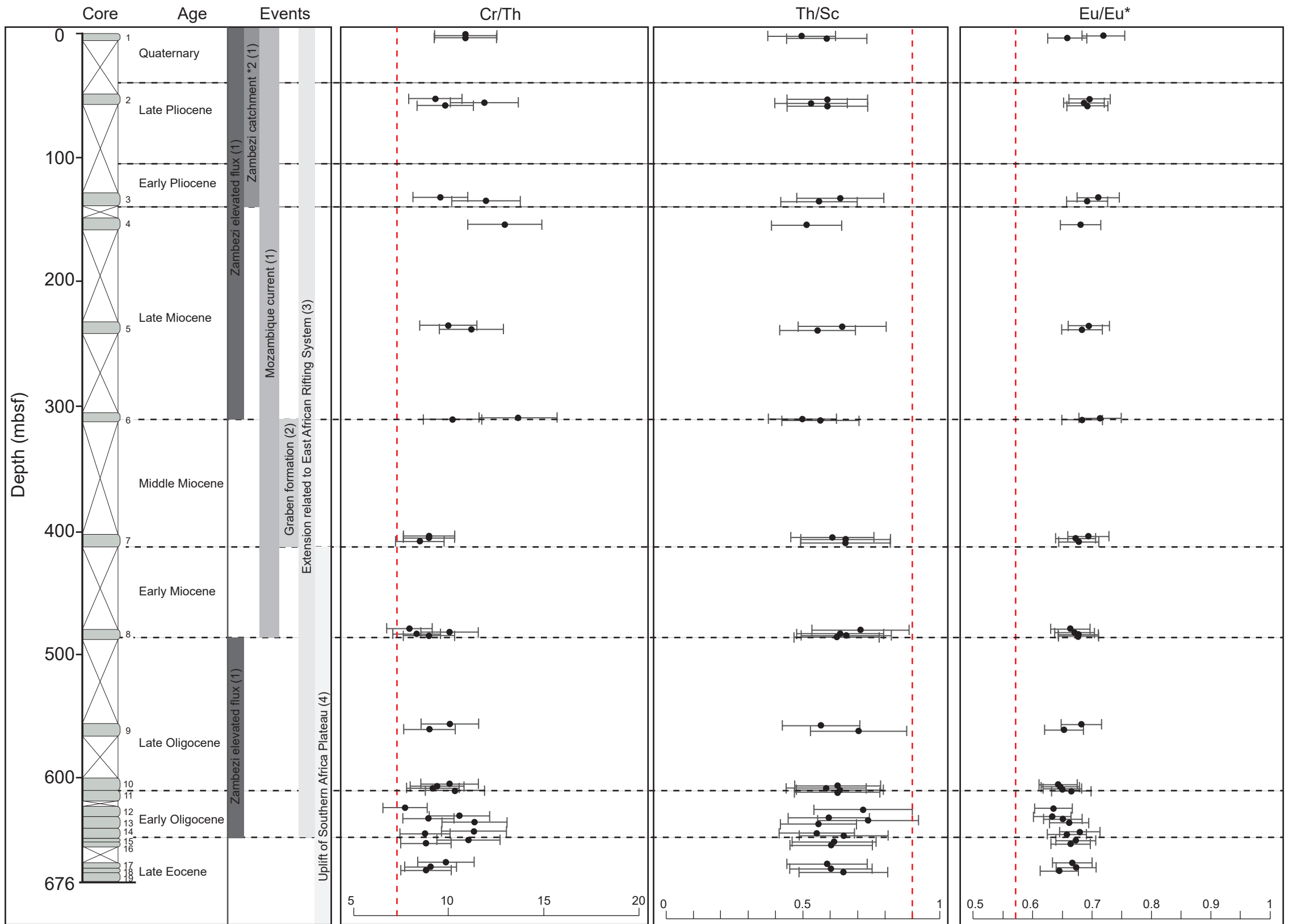


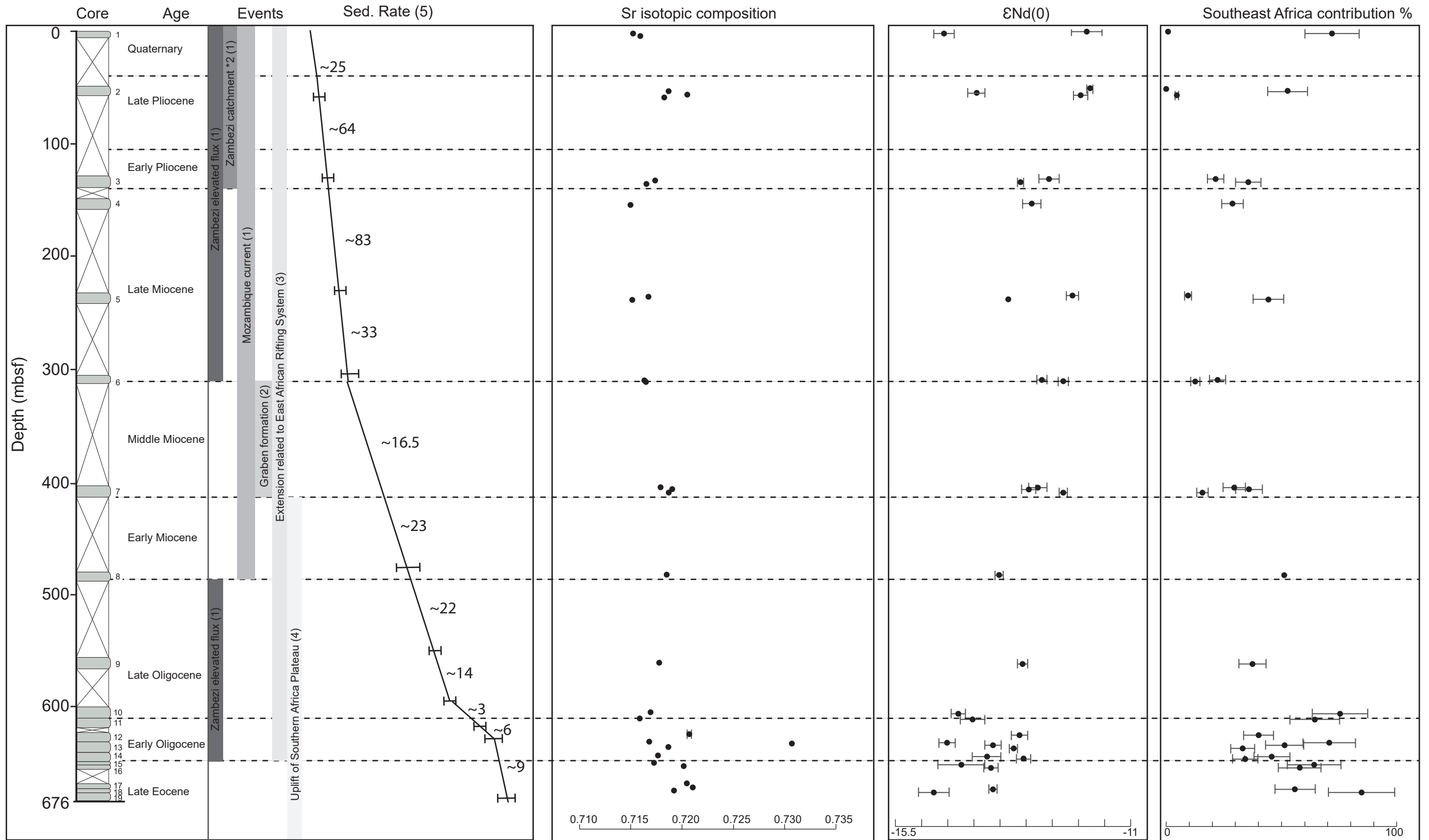
- Core tops (van der Lubbe et al., 2016)
- ▲ Core 64PE304-80/GIK16160-3 (van der Lubbe et al., 2016)
- VM 19-214 (Franzese et al. (2006)
- DSDP 25 Site 242 (this study)











Sample	Core	Age	top CSF-B [m]	bottom CSF-B [m]
1R2W	1	Quaternary	1.3667	1.38
1R4W	1	Quaternary	3.3467	3.36
2R1W	2	Late Pliocene	52.555	52.58
2R3W	2	Late Pliocene	55.56	55.58
2RCC	2	Late Pliocene	58	58
3R3W	3	Early Pliocene	132.06	132.08
3R5W	3	Early Pliocene	135.025	135.045
4R5W	4	Late Miocene	154.06	154.08
5R2W	5	Late Miocene	235.565	235.59
5R4W	5	Late Miocene	238.55	238.57
6R2W	6	Late Miocene	310.04	310.06
6R3W	6	Middle Miocene	311.5	311.52
7R2W	7	Middle Miocene	405.51	405.53
7R3W	7	Middle Miocene	407.02	407.04
7R5W	7	Middle Miocene	409.98	410
8R1W	8	Early Miocene	480.025	480.05
8R3W	8	Early Miocene	483.21	483.23
8R4W	8	Early Miocene	484.5	484.52
8R5W	8	Late Oligocene	486.05	486.07
9R2W	9	Late Oligocene	557.055	557.075
9R5W	9	Late Oligocene	561.51	561.53
10R3W	10	Late Oligocene	605.58	605.6
10R4W	10	Late Oligocene	607.5	607.52
10R5W	10	Late Oligocene	609	609.03
11RCCW	11	Early Oligocene	611	611
12R2W	12	Early Oligocene	625.01	625.035
13R1W	13	Early Oligocene	631.515	631.535
13R2W	13	Early Oligocene	633.48	633.5
13R4W	13	Early Oligocene	636.57	636.59
14R3W	14	Early Oligocene	644.01	644.03
14R4W	14	Early Oligocene	645.93	645.95
15R2W	15	Late Eocene	650.8044	650.8222
16R1W	16	Late Eocene	653.535	653.56
17R1W	17	Late Eocene	668.7067	668.72
18R1W	18	Late Eocene	672.5567	672.5667
19R3W	19	Late Eocene	675.34	675.3533

Table 1: Names, cores, ages and depths of sampled DSDP sediments ;
top CSF-B [m]: top core depth below sea floor in m;
bottom CSF-B [m]: bottom core depth below sea floor in m;

Sample		1R2W	1R4W	2R1W	2R3W	2RCC	3R3W*	3R5W	4R5W	5R2W	5R4W	6R2W	6R3W*	7R2W	7R3W	7R5W	8R1W	8R3W	8R4W	
Age		Quaternary	Quaternary	Late Pliocene	Late Pliocene	Late Pliocene	Early Pliocene	Early Pliocene	Late Miocene	Late Miocene	Late Miocene	Late Miocene	Middle Miocene	Middle Miocene	Middle Miocene	Middle Miocene	Early Miocene	Early Miocene	Early Miocene	
SiO2	%	43.07	46.14	47.04	45.62	45	39.13	45.61	44.79	46.4	45.55	46.88	41.16	46.92	45.17	46.86	46.03	44.91	46.28	
Al2O3	%	20.51	16.76	19.69	18.58	18.99	16.00	18.14	18.23	18.92	17.57	17.98	16.10	18.77	18.25	18.73	18.27	18.42	18.80	
Fe2O3	%	9.62	9.00	9.74	9.79	9.79	8.32	9.92	9.70	10.02	9.83	9.47	8.94	9.63	10.25	10.25	10.63	9.89	10.58	
MnO	%	0.06	0.04	0.04	0.04	0.04	0.04	0.04	0.04	0.04	0.04	0.04	0.05	0.05	0.06	0.05	0.06	0.05	0.06	
MgO	%	1.89	3.00	2.16	2.26	2.18	2.00	2.34	2.29	2.34	2.42	2.32	2.17	2.25	2.25	2.36	2.47	2.32	2.35	
CaO	%	1.15	1.47	1.59	1.19	3.10	9.98	1.23	1.18	1.13	1.13	1.24	7.73	1.49	1.15	1.20	1.07	1.15	1.03	
Na2O	%	0.11	0.14	0.21	0.17	0.18	0.16	0.13	0.11	0.11	0.11	0.15	0.14	0.14	0.15	0.13	0.13	0.09	0.13	
K2O	%	1.41	2.48	2.27	2.20	2.17	2.02	2.23	2.13	2.16	2.11	2.18	2.05	2.26	2.27	2.45	2.59	2.15	2.22	
TiO2	%	0.88	0.85	1.04	0.96	1.00	0.86	0.91	0.90	0.93	0.96	0.97	0.86	0.95	0.90	0.95	0.94	1.00	1.06	
P2O5	%	0.16	0.15	0.20	0.19	0.22	0.19	0.19	0.20	0.19	0.22	0.21	0.15	0.15	0.15	0.15	0.10	0.12	0.09	
LOI	%	20.18	19.24	17.22	18.41	17.43	21.10	18.45	19.59	18.15	19.30	19.03	20.42	16.86	18.70	16.55	16.82	18.72	16.93	
Total	%	99.03	99.28	101.20	99.39	100.09	99.78	99.19	99.17	100.36	99.21	100.47	99.77	99.47	99.25	99.68	99.10	98.80	99.51	
CIA		84	75	78	79	70	44	79	80	81	80	79	49	78	80	79	79	79	80	81
Al/Si		0.54	0.41	0.47	0.46	0.48	0.46	0.45	0.46	0.46	0.44	0.44	0.44	0.45	0.46	0.45	0.45	0.47	0.46	
Sc	ppm	22.66	20.44	23.08	20.88	22.26	18.83	20.95	20.44	22.1	20.94	19.53	19.64	22.52	20.79	22.18	23.33	22	24.23	
Rb	ppm	113.66	137.11	140.60	150.81	136.90	119.70	145.15	143.40	142.90	137.36	132.73	126.60	136.70	133.39	143.30	147.80	135.45	133.60	
Cs	ppm	5.99	6.35	6.21	6.99	6.04	5.19	6.67	6.45	6.12	5.83	6.29	5.11	5.68	5.51	5.94	6.07	6.46	5.91	
Ba	ppm	623.32	533.14	640.70	529.20	656.90	501.50	626.35	489.90	543.50	577.99	635.47	622.70	388.30	392.77	323.90	325.40	490.17	377.50	
Sr	ppm	86.40	90.32	110.80	88.55	166.50	425.90	100.58	91.53	92.31	88.18	98.68	317.10	108.30	81.78	90.69	86.85	85.45	92.94	
Th	ppm	11.23	12.00	13.60	11.07	13.13	11.99	11.72	10.50	14.23	11.60	9.73	11.08	13.69	13.65	14.54	16.58	14.00	15.96	
U	ppm	1.66	2.16	1.69	1.92	1.90	1.42	1.60	1.39	1.42	1.17	1.48	1.23	1.47	1.22	1.25	1.18	1.51	1.63	
Y	ppm	22.04	20.95	26.04	21.85	25.82	24.72	24.68	22.48	25.83	23.28	23.70	21.59	23.73	23.08	25.21	27.36	19.99	23.90	
Zr	ppm	78.91	67.84	75.21	75.36	75.06	64.25	79.10	72.82	79.31	71.64	78.40	65.03	72.85	71.15	70.27	70.14	66.79	76.93	
Nb	ppm	14.94	13.42	15.77	15.95	16.07	14.20	15.86	15.18	19.38	17.51	16.90	17.76	18.53	17.83	18.29	18.99	18.51	20.51	
Hf	ppm	2.24	2.06	2.24	2.23	2.24	1.97	2.34	2.19	2.45	2.03	2.21	1.99	2.21	2.10	2.17	2.12	2.05	2.18	
Cr	ppm	122.48	130.72	126.70	131.52	129.10	114.80	140.26	136.05	142.20	129.92	132.84	113.20	123.00	122.51	123.60	131.90	140.87	133.00	
V	ppm	119.93	127.45	137.20	127.20	137.00	114.30	131.59	126.71	150.00	120.43	127.78	114.10	127.50	113.74	130.40	124.50	149.69	139.60	
Co	ppm	17.23	28.75	20.90	20.91	22.25	18.55	22.09	21.13	21.66	20.17	20.60	19.12	31.08	23.51	26.57	28.51	23.72	23.14	
Cu	ppm	95.59	45.51	94.61	72.67	85.32	74.68	85.97	87.00	82.45	56.76	66.88	57.90	72.87	65.42	44.22	65.55	45.31	160.80	
Ni	ppm	76.27	78.14	66.29	65.31	70.88	56.78	64.60	63.66	62.57	61.48	61.48	63.59	84.71	75.69	78.44	87.66	79.90	79.63	
Zn	ppm	162.78	173.16	193.40	188.87	454.80	130.40	147.38	145.18	153.90	143.87	180.17	139.80	200.70	143.39	137.80	166.30	163.92	154.40	
La	ppm	32.39	37.05	42.88	37.79	44.50	40.47	41.44	40.50	45.41	44.17	38.88	38.70	44.44	47.24	47.64	51.71	45.38	47.65	
Ce	ppm	59.82	73.78	73.42	66.53	75.69	75.68	73.92	71.04	78.39	79.89	67.05	69.57	85.05	90.26	88.82	103.80	88.54	95.05	
Pr	ppm	6.75	8.62	9.55	8.29	9.81	9.46	9.07	8.72	10.10	9.59	8.28	8.73	10.18	10.49	10.73	11.73	10.16	10.36	
Nd	ppm	24.82	31.97	35.14	30.32	36.07	34.66	33.51	32.36	37.24	35.40	30.52	31.77	37.22	38.41	39.60	42.84	36.70	36.92	
Sm	ppm	4.77	5.98	6.48	5.69	6.69	6.46	6.40	6.04	6.82	6.67	5.66	5.87	6.95	7.04	7.26	8.04	6.67	6.62	
Eu	ppm	1.03	1.15	1.31	1.14	1.35	1.34	1.30	1.20	1.41	1.34	1.19	1.17	1.40	1.37	1.44	1.54	1.28	1.30	
Gd	ppm	3.99	4.75	5.11	4.49	5.31	5.12	5.16	4.81	5.64	5.36	4.61	4.67	5.48	5.49	5.81	6.27	5.13	5.19	
Tb	ppm	0.60	0.67	0.76	0.66	0.76	0.75	0.74	0.69	0.79	0.75	0.66	0.67	0.79	0.78	0.82	0.91	0.72	0.77	
Dy	ppm	3.68	3.84	4.51	3.86	4.53	4.41	4.34	3.98	4.58	4.30	3.94	4.00	4.50	4.51	4.64	5.19	4.09	4.39	
Ho	ppm	0.77	0.75	0.91	0.78	0.92	0.88	0.89	0.81	0.92	0.86	0.80	0.79	0.89	0.88	0.92	1.01	0.79	0.86	
Er	ppm	2.07	1.88	2.36	2.02	2.35	2.32	2.30	2.32	2.32	2.14	2.02	2.02	2.26	2.18	2.33	2.57	1.94	2.21	
Tm	ppm	0.29	0.25	0.34	0.28	0.34	0.32	0.31	0.28	0.31	0.29	0.27	0.28	0.30	0.30	0.32	0.35	0.26	0.31	
Yb	ppm	2.01	1.55	2.25	1.87	2.21	2.13	2.05	1.82	1.97	1.82	1.73	1.88	2.04	1.88	1.95	2.25	1.67	1.96	
Lu	ppm	0.30	0.22	0.33	0.27	0.33	0.31	0.30	0.29	0.29	0.26	0.27	0.28	0.29	0.29	0.29	0.32	0.23	0.29	
Ta	ppm	1.16	1.10	1.31	1.29	1.32	1.10	1.25	1.18	1.47	1.36	1.28	1.28	1.40	1.39	1.38	1.43	1.46	1.50	
Eu/Eu*		0.72	0.66	0.70	0.69	0.69	0.71	0.69	0.68	0.69	0.68	0.71	0.68	0.69	0.67	0.68	0.66	0.67	0.68	
ΩCe		0.97	0.99	0.87	0.91	0.87	0.93	0.92	0.91	0.88	0.94	0.90	0.91	0.96	0.98	0.95	1.02	0.99	1.03	
Cr/Th		10.91	10.89	9.32	11.89	9.83	9.57	11.97	12.95	9.99	11.20	13.65	10.22	8.98	8.98	8.50	7.96	10.06	8.33	
Th/Sc		0.50	0.59	0.59	0.53	0.59	0.64	0.56	0.51	0.64	0.55	0.50	0.56	0.61	0.66	0.66	0.71	0.64	0.66	

Table 2: Major and trace element concentrations of analyzed sediments. * denotes the samples that may have been affected by incomplete carbonate leaching leading to lower their CIA values

Sample		8R5W	9R2W	9R5W	10R3W	10R4W	10R5W	11RCCW	12R2W	13R1W	13R2W	13R4W	14R4W	14R3W	15RO2W	16R1W	17R1W	18R1W	19R3W
Age		Late Oligocene	Early Oligocene	Late Eocene															
SiO2	%	45.75	46.52	45.16	46	45.81	45.81	45.57	46.22	46.82	47.05	46.37	45.58	45.07	45.9	46.78	46.33	47.14	47.19
Al2O3	%	18.41	18.30	17.97	17.24	17.45	17.41	16.89	17.37	17.08	17.11	17.58	18.44	16.11	16.66	16.61	15.69	16.19	15.80
Fe2O3	%	10.27	9.78	10.50	9.41	10.69	10.58	9.58	10.54	10.45	9.84	9.85	9.54	9.00	9.70	10.06	9.34	10.02	9.52
MnO	%	0.06	0.05	0.04	0.04	0.05	0.05	0.04	0.05	0.04	0.04	0.04	0.04	0.06	0.04	0.04	0.07	0.07	0.05
MgO	%	2.27	2.47	2.25	2.65	2.69	2.68	2.63	2.86	2.87	2.93	2.63	2.34	2.91	2.81	3.33	3.37	3.56	3.75
CaO	%	1.33	1.10	0.99	1.36	1.36	1.36	1.41	1.23	1.45	1.37	1.35	1.28	4.40	1.33	1.23	3.08	1.64	1.39
Na2O	%	0.13	0.11	0.10	0.12	0.14	0.14	0.10	0.13	0.12	0.16	0.14	0.11	0.20	0.13	0.16	0.19	0.16	0.19
K2O	%	2.25	2.39	2.26	2.21	2.52	2.45	2.34	2.68	2.61	2.74	2.48	2.05	2.61	2.62	2.92	3.01	2.88	2.84
TiO2	%	0.98	0.95	0.93	0.91	0.95	0.90	0.88	0.85	0.88	0.87	0.87	0.89	0.89	0.84	0.87	0.87	0.89	0.89
P2O5	%	0.13	0.14	0.13	0.13	0.12	0.13	0.12	0.11	0.15	0.13	0.15	0.20	0.15	0.12	0.14	0.16	0.18	0.11
LOI	%	17.00	16.93	18.82	19.28	16.89	17.24	19.03	16.79	18.40	17.24	19.27	19.72	18.04	19.09	17.03	17.35	17.15	18.39
Total	%	98.59	98.74	99.14	99.34	98.68	98.75	98.59	98.82	100.86	99.47	100.71	100.17	99.41	99.23	99.17	99.47	99.87	100.12
CIA		78	79	80	77	76	77	76	75	75	77	77	80	59	75	75	63	72	73
Al/Si		0.46	0.45	0.45	0.42	0.43	0.43	0.42	0.43	0.41	0.41	0.43	0.46	0.41	0.41	0.40	0.38	0.39	0.38
Sc	ppm	22.27	23.12	20.36	21.62	24.06	23.5	20.97	22.46	20.99	20.84	19.78	20.25	21.22	20.22	23.86	21.87	23.37	22.71
Rb	ppm	138.70	137.60	137.04	137.63	140.20	144.30	134.18	140.10	120.69	148.40	126.12	112.33	143.00	133.46	146.70	153.00	144.10	131.70
Cs	ppm	5.95	5.79	5.67	6.84	6.22	6.63	6.57	6.47	6.42	6.84	6.62	5.98	6.48	6.33	6.41	6.50	6.48	6.62
Ba	ppm	358.60	499.50	516.45	456.47	380.90	391.40	512.63	456.70	402.00	468.20	514.33	579.55	533.50	453.66	407.50	393.90	390.10	453.60
Sr	ppm	104.00	99.63	78.67	91.66	93.38	96.21	96.85	81.88	81.38	86.95	81.01	87.41	174.50	82.95	84.60	134.60	90.50	76.94
Th	ppm	13.88	13.10	14.33	13.56	14.08	14.93	13.12	16.18	12.48	15.39	11.02	11.15	13.78	12.42	14.40	12.87	14.08	14.72
U	ppm	1.24	1.56	1.27	1.59	1.23	1.51	1.90	1.79	1.71	1.87	1.66	1.80	1.76	1.66	1.05	1.42	1.03	1.16
Y	ppm	21.99	25.04	19.56	23.63	20.26	22.87	22.12	23.90	19.80	22.88	19.30	21.44	23.10	22.28	27.66	24.62	27.08	23.45
Zr	ppm	75.77	79.28	70.46	80.09	56.36	58.51	64.01	67.01	62.24	68.30	65.44	72.80	65.31	71.05	69.47	71.39	73.78	70.31
Nb	ppm	20.13	20.35	18.44	14.21	14.32	14.32	14.11	14.69	14.31	14.53	13.20	14.18	14.00	13.44	13.71	13.95	14.20	13.50
Hf	ppm	2.18	2.33	2.04	1.85	1.78	1.90	2.00	2.17	1.92	2.18	1.99	2.04	2.04	2.16	2.20	2.14	2.24	2.10
Cr	ppm	124.60	132.00	129.06	136.43	132.40	137.10	135.61	125.00	132.05	137.70	125.25	126.48	120.90	137.22	127.00	127.00	127.60	129.90
V	ppm	121.50	122.00	115.96	137.25	130.50	133.30	124.30	118.20	130.30	124.10	116.02	119.78	121.50	112.22	132.40	118.40	102.40	118.51
Co	ppm	25.64	39.19	23.23	25.61	26.57	26.02	24.29	23.45	23.95	26.54	26.22	24.12	24.42	28.77	24.38	34.66	25.09	27.75
Cu	ppm	83.74	55.63	44.22	54.41	54.62	53.41	45.92	65.63	45.00	55.24	58.82	78.34	60.40	47.69	118.20	44.09	89.16	47.69
Ni	ppm	80.30	104.40	75.74	79.07	79.65	81.82	75.79	73.67	71.72	82.90	75.35	69.75	71.71	87.57	86.41	91.79	84.26	90.56
Zn	ppm	150.70	160.00	150.15	170.59	149.70	155.80	216.52	138.50	143.96	146.60	143.63	134.73	137.60	145.06	160.80	151.30	155.00	167.83
La	ppm	46.34	45.19	45.59	44.39	42.67	46.04	41.29	45.23	39.35	40.17	35.49	35.62	39.25	37.38	45.88	40.82	43.79	42.87
Ce	ppm	89.02	87.47	87.68	86.10	79.35	87.67	82.46	83.48	70.52	74.42	64.85	65.41	73.99	73.44	83.36	74.53	81.68	75.85
Pr	ppm	10.22	10.15	10.14	10.10	9.65	10.30	9.60	10.25	8.77	9.38	7.69	7.89	9.22	8.72	10.35	9.46	10.15	9.66
Nd	ppm	36.98	37.16	36.31	37.18	35.04	37.48	35.67	37.17	32.11	34.48	28.27	28.97	33.78	32.40	38.05	34.83	37.54	35.19
Sm	ppm	6.86	6.86	6.52	6.93	6.46	6.94	6.64	6.75	6.00	6.51	5.33	5.41	6.48	6.01	7.18	6.57	7.14	6.57
Eu	ppm	1.33	1.36	1.21	1.30	1.19	1.30	1.27	1.25	1.09	1.22	1.03	1.09	1.22	1.18	1.39	1.27	1.41	1.24
Gd	ppm	5.29	5.44	4.91	5.52	4.88	5.35	5.13	5.33	4.62	5.06	4.23	4.40	4.96	4.82	5.66	5.18	5.76	5.22
Tb	ppm	0.77	0.80	0.70	0.78	0.71	0.78	0.73	0.77	0.65	0.73	0.61	0.63	0.73	0.70	0.84	0.75	0.84	0.75
Dy	ppm	4.29	4.55	4.00	4.52	3.92	4.42	4.22	4.38	3.69	4.15	3.47	3.76	4.22	4.00	4.88	4.41	4.92	4.31
Ho	ppm	0.83	0.90	0.76	0.90	0.75	0.84	0.82	0.85	0.71	0.80	0.68	0.75	0.81	0.79	0.96	0.85	0.95	0.85
Er	ppm	2.11	2.30	1.89	2.25	1.92	2.15	2.06	2.14	1.81	1.98	1.75	1.91	2.06	2.00	2.48	2.20	2.45	2.18
Tm	ppm	0.29	0.31	0.25	0.30	0.26	0.30	0.27	0.29	0.24	0.26	0.24	0.26	0.28	0.26	0.33	0.30	0.34	0.29
Yb	ppm	1.90	2.00	1.58	1.96	1.66	1.90	1.74	1.87	1.50	1.65	1.48	1.65	1.84	1.68	2.18	1.94	2.16	1.86
Lu	ppm	0.27	0.30	0.22	0.27	0.24	0.27	0.26	0.27	0.21	0.24	0.22	0.24	0.27	0.25	0.31	0.28	0.31	0.27
Ta	ppm	1.41	1.52	1.40	1.15	1.15	1.17	1.16	1.20	1.15	1.16	1.09	1.13	1.13	1.14	1.12	1.11	1.10	1.15
Eu/Eu*		0.68	0.68	0.65	0.64	0.65	0.65	0.66	0.63	0.63	0.65	0.66	0.68	0.66	0.67	0.66	0.67	0.67	0.64
ΩCe		0.99	0.98	0.98	0.98	0.94	0.97	1.00	0.93	0.91	0.92	0.95	0.94	0.94	0.98	0.92	0.91	0.93	0.90
Cr/Th		8.98	10.08	9.00	10.06	9.40	9.18	10.34	7.73	10.58	8.95	11.37	11.34	8.77	11.05	8.82	9.87	9.06	8.82
Th/Sc		0.62	0.57	0.70	0.63	0.59	0.64	0.63	0.72	0.59	0.74	0.56	0.55	0.65	0.61	0.60	0.59	0.60	0.65

Table 2 (end)

Sample	age	$^{147}\text{Sm}/^{144}\text{Nd}$	TDm	$^{143}\text{Nd}/^{144}\text{Nd}$	$\pm 2\sigma$	$\epsilon_{\text{Nd}(0)}$	$\pm 2\sigma$	$^{87}\text{Sr}/^{86}\text{Sr}$	$\pm 2\sigma$	% SeA	Laboratory
1R2W	Quaternary			0.512031	0.000015	-11.8	0.3	0.715226	0.000009	0.8	GET
1R4W	Quaternary			0.511891	0.000010	-14.6	0.2	0.715925	0.000014	71.9	GET
2R1W	Late Pliocene	0.1085	1.45	0.512034	0.000003	-11.8	0.1	0.71869	0.000010	0.0	Geochronos
2R3W	Late Pliocene	0.1035	1.54	0.511923	0.000008	-13.9	0.2	0.72052	0.000090	52.8	Geochronos
2RCC	Late Pliocene	0.1079		0.512025	0.000007	-12.0	0.1	0.71826	0.000010	4.6	Geochronos
3R3W	Early Pliocene	0.1077	1.5	0.511994	0.000010	-12.6	0.2	0.71737	0.000080	21.4	Geochronos
3R5W	Early Pliocene	0.1060	1.51	0.511966	0.000003	-13.1	0.1	0.7165	0.000020	35.6	Geochronos
4R5W	Late Miocene	0.1012	1.43	0.511977	0.000009	-12.9	0.2	0.714955	0.000015	28.7	Geochronos
5R2W	Late Miocene	0.1069	1.45	0.512017	0.000006	-12.1	0.1	0.71671	0.000010	9.5	Geochronos
5R4W	Late Miocene			0.511954		-13.3	0.0	0.715143	0.000010	44.3	GET
6R2W	Late Miocene	0.1068	1.49	0.511987	0.000005	-12.7	0.1	0.71632	0.000010	22.3	Geochronos
6R3W	Middle Miocene	0.1063	1.46	0.512008	0.000005	-12.3	0.1	0.71647	0.000040	12.6	Geochronos
7R2W	Middle Miocene	0.1068	1.5	0.511983	0.000009	-12.8	0.2	0.7179	0.000010	29.5	Geochronos
7R3W	Middle Miocene	0.1064	1.51	0.511974	0.000007	-13.0	0.1	0.71903	0.000004	35.9	Geochronos
7R5W	Middle Miocene	0.1080	1.48	0.512008	0.000004	-12.3	0.1	0.7187	0.000090	15.7	Geochronos
8R1W	Early Miocene										
8R3W	Early Miocene	0.1005	1.47	0.511945	0.000004	-13.5	0.1	0.71848	0.000020	51.2	Geochronos
8R4W	Early Miocene										
8R5W	Late Oligocene										
9R2W	Late Oligocene										
9R5W	Late Oligocene	0.1059	1.51	0.511968	0.000005	-13.1	0.1	0.71777	0.000080	37.4	Geochronos
10R3W	Late Oligocene			0.511905	0.000007	-14.3	0.1	0.716928	0.000018	75.4	GET
10R4W	Late Oligocene										
10R5W	Late Oligocene										
11RCCW	Early Oligocene			0.511919	0.000012	-14.0	0.2	0.715875	0.000012	64.4	GET
12R2W	Early Oligocene	0.1059	1.51	0.511965	0.000008	-13.1	0.2	0.7207	0.000210	40.1	Geochronos
13R1W	Early Oligocene			0.511894	0.000008	-14.5	0.2	0.71682	0.000018	70.7	GET
13R2W	Early Oligocene	0.1074	1.57	0.511939	0.000008	-13.6	0.2	0.7307	0.000100	51.4	Geochronos
13R4W	Early Oligocene	0.1038	1.49	0.511959	0.000004	-13.2	0.1	0.71866	0.000050	33.2	Geochronos
14R4W	Early Oligocene	0.1076	1.58	0.511933	0.000014	-13.8	0.3	0.717634	0.000012	45.9	Geochronos
14R3W	Early Oligocene	0.1084	1.54	0.511969	0.000007	-13.1	0.1			34.3	Geochronos
15R02W	Late Eocene			0.511908	0.000023	-14.2	0.4	0.717244	0.000014	64.2	GET
16R1W	Late Eocene	0.1028	1.51	0.511937	0.000007	-13.7	0.1	0.72016	0.000020	57.9	Geochronos
17R1W	Late Eocene							0.72048	0.000020		GET
18R1W	Late Eocene	0.1091	1.59	0.511939	0.000004	-13.6	0.1	0.72104	0.000010	55.9	Geochronos
19R3W	Late Eocene			0.511881	0.000015	-14.8	0.3	0.719207	0.000010	84.7	GET

Table 3: Nd-Sr isotopic systematics of the analyzed sediments; SeA: Southeast Africa; GET: Géosciences Environnement Toulouse and Geochronos;

Age	CIA	N	S.D.	C.I.	Eu/Eu*	N	S.D.	C.I.	QCe	N	S.D.	C.I.	Cr/Th	N	S.D.	C.I.	Th/Sc	N	S.D.	C.I.	δ_{OBS}	N	S.D.	C.I.	$^{87}\text{Sr}/^{86}\text{Sr}$	N	S.D.	C.I.	% SeA	S.D.
Quaternary	80	2	7	10	0.69	2	0.04	0.06	0.98	2	0.01	0.02	10.90	2	0.01	0.02	0.54	2	0.06	0.09	-13.2	2	1.9	2.7	0.715576	2	0.000494	0.000685	36.4	50.3
Late Pliocene	76	3	5	6	0.69	3	0.00	0.01	0.88	3	0.02	0.02	10.34	3	1.36	1.54	0.57	3	0.03	0.04	-12.6	3	1.2	1.4	0.719157	3	0.001200	0.001358	19.1	29.2
Early Pliocene	61	2	25	34	0.70	2	0.01	0.02	0.93	2	0.01	0.01	10.77	2	1.70	2.35	0.60	2	0.05	0.08	-12.8	2	0.4	0.5	0.716935	2	0.000615	0.000853	28.5	10.0
Late Miocene	80	4	1	1	0.69	4	0.01	0.01	0.91	4	0.02	0.02	11.95	4	1.66	1.63	0.55	4	0.07	0.06	-12.8	4	0.5	0.5	0.715782	4	0.000865	0.000847	26.2	14.5
Middle Miocene	71	4	15	14	0.68	4	0.01	0.01	0.95	4	0.03	0.03	9.17	4	0.73	0.72	0.62	4	0.04	0.04	-12.6	4	0.3	0.3	0.718025	4	0.001140	0.001117	23.4	11.1
Early Miocene	80	3	1	1	0.67	3	0.01	0.01	1.01	3	0.02	0.02	8.78	3	1.12	1.27	0.67	3	0.04	0.04	-13.5	1	N.A.		0.718460	1	N.A.		51.2	N.A.
Late Oligocene	78	6	2	1	0.66	6	0.02	0.01	0.97	6	0.02	0.01	9.45	6	0.50	0.40	0.62	6	0.05	0.04	-13.7	2	0.9	1.2	0.717349	2	0.000595	0.000825	56.4	26.9
Early Oligocene	74	7	7	5	0.65	7	0.02	0.01	0.94	7	0.03	0.02	9.87	7	1.40	1.04	0.63	7	0.07	0.05	-13.6	7	0.5	0.4	0.720065	6	0.005468	0.004375	48.6	14.6
Late Eocene	72	5	5	4	0.66	5	0.01	0.01	0.93	5	0.03	0.03	9.52	5	0.95	0.84	0.61	5	0.02	0.02	-14.1	4	0.5	0.5	0.719626	5	0.001489	0.001305	65.7	13.2

Table 4: mean and standard deviation (S.D) of selected proxies and isotopic ratios. N: number of sample used to calculate the mean and standard deviation for each age period. C.I. : Confidence Interval calculated using a normal law at 95%. N.A.: not applicable. SeA: Southeast Africa